

A far IR study of the CfA Seyfert sample: I. The data ¹

A. M. Pérez García^{1,2}, J. M. Rodríguez Espinosa ¹

¹Instituto de Astrofísica de Canarias, E-38200 La Laguna (Tenerife), Spain

² Isaac Newton Group, La Palma, Spain

Electronic mail: apg@iac.es, jre@iac.es

Received _____; accepted _____

arXiv:astro-ph/0003349v1 23 Mar 2000

¹Based on observations with ISO, an ESA project with instruments funded by ESA Member States (especially the PI countries: France, Germany, the Netherlands and the United Kingdom) and with the participation of ISAS and NASA.

ABSTRACT

We present mid and far IR ISO data of the CfA Seyfert galaxy sample. These data allow a detailed study of the far IR Spectral Energy Distribution (SED) of these galaxies. A Bayesian inversion method has been used to invert the SED of these sources yielding two fundamental results, namely, that the mid and far IR SED of Seyfert galaxies can be explained solely through thermal reradiation of high energy photons by dust, and that this thermal emission is made up of two or three different independent components, a warm, a cold and a very cold dust component. These thermal components have been readily explained as produced respectively by warm dust heated by either the active nucleus or by circumnuclear starbursts, cold dust heated by star forming region in the galaxy disk, and very cold dust heated by the general interstellar radiation field. Comparisons between the parameters obtained from the analysis of the IR SEDs (fluxes, temperatures, luminosities) have been made. Our results suggest that the emission in the mid IR is anisotropic and the differences found between Seyfert 1 and Seyfert 2s can be explained with thin molecular tori models.

1. Introduction

The origin of the IR emission from Seyfert galaxies has been a matter of discussion since the early work of Rieke & Low (1972); Stein (1975); Rieke (1978); Neugebauer (1978), and others. These authors found an emission excess between 3 and 5 μm in Seyfert galaxies, that originated a strong controversy between those who supported that the emission was non thermal and those who defended that the excess was emission from dust heated by the nucleus. The use of efficient instruments to observe at 10 μm , and especially the pioneering work at the far IR carried out from the Kuiper Airborn Observatory (KAO) showed the importance of the mid and far IR emission to quantify the bolometric luminosity of Seyfert galaxies (Telesco & Harper 1980; Smith et al. 1983). However, it was the IRAS satellite that provided an extensive set of IR data for a large number of galaxies, from which it was shown that Seyfert galaxies are indeed strong far IR emitters (Rodríguez Espinosa, Rudy & Jones 1987; Edelson, Malkan & Rieke 1987; Spinoglio et al. 1995).

The IRAS satellite was key to the understanding of the importance of the IR emission to the total luminosity of active galaxies. However the IRAS data alone are not sufficient to clarify the nature of the IR emission, as there are measurements only at a limited number of wavebands preventing a good definition of the shape of the Spectral Energy Distribution (SED) at mid and far IR wavelength (see, e.g., Telesco 1988; 1990; Bregman 1990). A proper characterization of the mid and far SED is essential to understand the emission mechanisms that produce the high output of Seyfert galaxies in the IR. Recent studies have discussed the origin of the IR emission suggesting that it is of thermal origin. For example Giuricin, Mardirossian & Mezzetti (1995) have studied a complete sample of Seyfert galaxies at 10 μm and propose that the emission is due to thermal reemission by dust. Bonatto & Pastoriza (1997), based on color studies of IRAS data from diverse Seyfert samples, find that the colors obtained can be explained with a combination of dust heated by the nucleus plus cold dust in the host galaxy. Siebenmorgen et al. (1997) show that the SED at IR and milimetric wavelengths can be modeled assuming that the dust heated by a central source dominates the luminosity output of these objects. Maiolino et al. (1998) confirmed this last result finding, in their high resolution IR images of the Circinus galaxy, an unresolved source, with size < 1 pc, that is reprocessing the nuclear output via dust reradiation. Rigopoulou et al. (1997) have observed a sample of AGN in the CO mm line suggesting that the far IR emission of Seyfert galaxies is thermal, based on three different evidences: the correlation found between the far IR and the CO emission, the dependence of the far IR emission to hydrogen molecular mass ratio with dust temperature, and the similarity of the profile shape of the CO and HI lines.

Another important issue is the understanding of the differences between the two Seyfert types. According to the unified models, Seyfert 2 nuclei are intrinsically similar to Seyfert 1 nuclei, the differences observed being due solely to geometrical effects. In Seyfert 2, neither the broad line region nor the optical, UV and soft X ray continuum can be observed directly because the central region is obscured by intervening material in the line of sight. Some authors argue that this material forms a sort of disc or torus of molecular material. This disc or torus is thought to be responsible for the collimation of radiation and the observed anisotropies, i.e., biconic structures in emission line images (Simpson et al. 1997; Wilson et al. 1993) or highly collimated jets. It is expected that at sufficiently long wavelengths the optical depth of the torus would decrease and the differences between the two Seyfert types should disappear. Several tests have been made to ascertain the presence of these molecular tori (Heckman 1995; Pier & Krolik 1993). These obscuring tori have been theoretically modeled by Pier & Krolik (1992) and Granato & Danese (1994) among others, predicting that the mid IR optical depth is still considerable, thus it should be expected that Seyfert 1s are more luminous than Seyfert 2s in the mid IR.

In this work, we make an attempt to understanding the origin of the mid and far IR emission from Seyfert galaxies through the study of their spectral energy distributions (SED). We present ISO data of the entire CfA Seyfert sample (Huchra & Burg 1992), consisting of 25 Seyfert 1 and 22 Seyfert 2, plus a LINER. Section 2 describes the observations. Section 3 presents the separation of the Spectral Energy Distributions in thermal components by means of the Inverse Planckian Transform. Section 4 describes the thermal emission components obtained from the inversion and in Section 5 we perform a statistical analysis of the parameters obtained and discuss the differences between the two Seyfert types.

As the CfA Seyfert sample is a complete sample of Seyfert galaxies we expect that the results obtained here are statistically significant for all Seyfert galaxies and certainly suggestive for other classes of AGNs.

2. The data

Observations of the CfA Seyfert sample have been carried out with the Infrared Space Observatory (ISO; Kessler et al. 1996) through filters at 16, 25, 60, 90, 120, 135, 180 and $200\mu\text{m}$. NGC 1068 was also observed at 4.9, 7.3 and $11.5\mu\text{m}$. The filter set was chosen to achieve good coverage in wavelength while producing a good sampling of the SEDs. The ISOPHOT instrument (Lemke et al. 1996) was used in the PHT-P and PHT-C configurations, with the P1, P2, C100 and C200 detectors. P1 and P2 are single element photodiodes. C100 is an array of 3x3 pixels, each one projecting onto 45 arcsec in the sky, while

C200 is a 2x2 pixel array, each pixel projecting onto 89.4 arcsec in the sky. Integration times were calculated from the signal/noise ratio estimates produced by the ISOPHOT simulator based on interpolations and extrapolations of the IRAS data. The PHT-P observations were done in chopping mode through a 120 or 180 arcsec aperture depending on the size of the objects. The PHT-C observations were done in staring mode. In this case, to set the background level, an empty area adjacent to the source was observed prior to the actual source and with identical instrumental settings. For NGC 1068 we have done maps with C100, at 60 and 105 μm , moving by half a pixel ($23''$) between two contiguous map positions. Four additional objects (NGC 3079, NGC 3227, NGC 4051 and NGC 4151) have been mapped at 90 μm with the C100 array. Details of the mapping observations of these four galaxies are given in Pérez García, Rodríguez Espinosa & Fuensalida (2000).

The data reduction was done with the help of the PHT-Interactive Analysis (PIA) V.7.0 tool. PIA first deglitches the data eliminating the cosmic rays and others spurious effects, then corrects for non-linear effects taking into account both the dynamic range of the detectors and the flux level of the observed sources. To determine the signal PIA linearizes the integration ramps, and corrects for detector drifts. The background subtraction is achieved by repeating the PIA reduction process for the background measurements files, which are then subtracted from the object files. It is also necessary to correct for the PSF fraction that is not seen by the detector (see Lemke et al. 1996). This factor varies with wavelength, hence the actual correction factor for each filter is built-in in a PIA table. The flux calibration is performed using the standard calibration of PIA 7.0. For the PHT-P measurements the process is similar except that the background subtraction is performed automatically from the chopped measurements and the flux calibration is done through the use of the internal FCS (Fine Calibration Source; Lemke et al. 1996) since it provides a better match with the actual intensity of the sources. Note that the P detector response is very dependent on the intensity of the source being observed.

The photometric uncertainties are small varying between 1% for the objects with higher signal/noise ratio and 15% for the weakest objects. The final uncertainties are however dominated by the uncertainties in the flux calibration. The calibration factors have kept improving as the detector and instrument characteristics have become better known, although there are still some residual effects (non linearity of detectors) that are yet not adequately modelled. As of this writing, the uncertainty of the calibration is equal or better than 30%. Therefore, throughout this paper, we adopt a conservative uncertainty of 30%.

The fluxes for the observed objects are given in Table 1 and 2. Fluxes are in Janskys. Some objects

could not be observed in some or all of the filters for various reasons. These are also given in Table 1.

Figure 1 shows the Spectral Energy Distributions (SEDs) of the observed objects. The ISO data have been plotted together with IRAS data (Edelson, Malkan & Rieke 1987) at 12, 25, 60 and 100 μ m showing that the agreement of the ISO and IRAS data is very good in most cases.

EDITOR: PLACE TABLE 1 HERE.

EDITOR: PLACE TABLE 2 HERE.

3. The inversion of the SEDs

It can be seen in fig. 1 that the SEDs describe a well defined energy range with a steady increase from the near IR on to a maximum between 90 and 135 μ m and the start of a decline toward longer wavelengths. Several results like those mentioned in the introduction point to the mid and far-IR emission of Seyfert galaxies being of thermal origin. Furthermore, we have shown that the SED of a few Seyfert galaxies can be explained as emission produced by two emissivity weighted blackbodies (Rodríguez Espinosa et al. 1996).

EDITOR: PLACE FIGURE 1 HERE.

However, rather than proceeding with a plain fit of a “ad hoc” number of black bodies, we have preferred to use an inversion method to analyze the SEDs of the galaxies in the sample. This has the advantage that no assumptions have to be made as to the number or location of the sources responsible for the observed spectrum. In particular, we have used an Inverse Planckian Transform algorithm, that employs an emissivity ($\epsilon \propto \lambda^{-1.5}$) weighted Planck function kernel to switch from frequency space to the temperature domain, hence revealing the temperature distribution of the sources that originate the observed SEDs. The method applies Bayes theorem of conditional probability and the Richardson-Lucy iteration algorithm which converges quickly to a optimum result. To increase the number of data points used in the inversion algorithm, whenever available, we have added the four IRAS band fluxes at 12, 25, 60 and 100 μ m as given by Edelson, Malkan & Rieke (1987). Furthermore, to avoid boundary convergence problems in the inversion algorithm we have used 10 μ m ground-based data from several authors (Rieke 1978; Edelson,

Malkan & Rieke 1987; Maiolino et al 1995), and 1.3 mm upper limit data from Edelson, Malkan & Rieke (1987). These additional data have been used solely for the purpose of constraining the inversion algorithm at the borders of the wavelength range of interest. Details of this method are given in Salas (1992) and in Pérez García, Rodríguez Espinosa, & Santolaya Rey (1998) and are not repeated here.

Figure 2 shows the results obtained after application of the Inverse Planckian Transform to the SEDs of the CfA Seyfert galaxies observed. For each object, the upper pannel in Figure 2 plots the ISO data (triangles) and the IRAS data (filled squares) and the best fit to the mid and far IR data in heavy black, with the different spectral components contributing to the fit printed in dashed lines; the bottom pannel shows the temperature spectrum that produces these components.

EDITOR: PLACE FIGURE 2 HERE.

It is important to note that the temperature spectra obtained in this way are continuous. Further, the spectral temperatures of the dust grains group themselves in discrete and well defined features that we have called components. These components can be described by their peak temperature. Figure 2 shows that 34 out of the 40 galaxies for which we have obtained good temperature spectra show three temperature components: a warm component with central temperature $T \sim 150$ K, a cold component with $T \sim 40-70$ K, and a colder component with $T \sim 15-25$ K. The remaining 6 objects show only two components, although in NGC 1068 when the short wavelength data are added a third component is recovered. Table 3 shows the peak temperatures of these thermal components for each object. This table also gives the spectral and morphological type for each object. These results confirm the analysis made before for a few objects of the same sample (Pérez García, Rodríguez Espinosa, & Santolaya Rey 1998).

The fits obtained from the inversion are, in general, very good. In some cases, weak objects or objects with low signal to noise ratios, the uncertainty in the inversion is higher. For some objects, we have rejected some measurements (the flux at $120\mu\text{m}$ of NGC 4235, and the fluxes at $90\mu\text{m}$ of Mrk 270, Mrk 461 and 1614+35) because these data points do not follow the shape of the SEDs defined by the rest of the measurements. In all of these cases the rejected measurement is very noisy. Four other objects (Mrk 590, Mrk 573 and Mrk 841) have not been measured at long wavelengths ($>90\mu\text{m}$), because they are below the sensitivity limit for detection with ISO.

Nevertheless, the method still finds three components for three out of the except for NGC 1068, that will be analyzed in a separate section. four objects. For Mrk 590, the inversion does not converge.

In four of the objects, the warm component peak temperature obtained from the inversion is not high enough to fit the data. These four objects are Mrk 335, NGC 5273, Mrk 1243 and IZw1. Both in Mrk 335 and in NGC 5273 it can be due to the low signal to noise ratio of the data. NGC 5273 shows a discrepancy between the IRAS value at $12\ \mu\text{m}$ and the ISO value at $16\ \mu\text{m}$ (again very likely due to the low signal to noise ratio of the ISO data point) that prevents a good fit to the data. Mrk 1243 has only three data points in the hot part of the spectrum. IZw1 is a special case, since the short wavelength data are of good signal to noise ratio, however it is not detected at $200\ \mu\text{m}$ and the flux at $180\ \mu\text{m}$ is rather low. The fall of the signal at longer wavelengths is fast enough to explain that the object is not detected at $200\ \mu\text{m}$. Figure 2 shows that the SED of IZw1 if made of just two components does not account for all of the observed emission. If we subtract this initial two-component fit from the actual SED, the residual seems to correspond to yet one third hotter thermal component. The inversion method does not succeed at identifying completely this third component, due to the temperature of this third component being too high, therefore only a small fraction of the energy within this third component falls within the range of wavelength studied. The shape of the residual is however similar to the other two components, a clear hint of the existence of yet another thermal component with a peak temperature of $\sim 300\ \text{K}$. This temperature is the highest temperature found among all of the SEDs. The cold and very cold components also have peak temperatures higher than the corresponding components of the SEDs of the rest of the CfA sample. IZw1 is one of the more distant and brighter Seyfert galaxies known. Its different spectroscopic characteristics of line width and line ratios were pointed out by Osterbrock and Pogge (1985) and Goodrich (1989). Recently, several authors have pointed out the different nature of IZw1. For example, the optical and X-ray spectra are steeper in IZw1 than in normal Seyfert 1 and 2. Indeed IZw1 shows fast and large amplitude variability in its X-ray emission (see Halpern & Moran 1998 and references there in), and is possibly better associated with the broad line quasars (Boroson & Meyers 1992; Lawrence et al. 1997).

4. The dust components

The inversion method assigns to each dust component a range of temperature, i.e., the dust grains have temperatures ranging between a minimum and a maximum temperature. This is indeed an expected and physically meaningful result, as the dust closer to the source or sources of radiation will be warmer than the dust farther away. The existence of temperature components indicates that there are well defined sources with well defined temperature profiles which must be the result of well defined physical scenarios

existing in these objects. From the temperature spectra, we can calculate the flux that each dust component contributes to the total mid and far IR emission. For each component, the flux is obtained by integration of the temperature spectrum over the relevant range of temperatures:

$$F_i = \int_{T_{min_i}}^{T_{max_i}} \Psi(T) dT \quad i = 1, 2, 3 \quad (1)$$

where T_{min_i} and T_{max_i} are the extreme values of the temperature range that defines each component, and $\Psi(T)$ is the temperature distribution obtained from the inversion process. Table 4 shows the fluxes obtained in this way for each component and the total flux for each object. The comparison between the far IR IRAS fluxes (FIR), as calculated from the values at 60 and 100 μm (Lonsdale et al. 1984) and the sum of the cold and very cold components calculated here is in good agreement. The luminosities for each of the components are shown in Table 5. We have used $H_0 = 75 \text{ Km s}^{-1} \text{ Mpc}^{-1}$ throughout this paper.

The key point now is whether these emission components can be physically explained within a sensible scenario. In what follows we review the pieces of evidence that we have for explaining each of components:

a) In a previous paper Rodríguez Espinosa & Pérez García (1997) were able to use optical R band images of a subset of low redshift Seyferts of the present sample to separate the fluxes from the central region from those of the galaxy disks. We found a very good correlation between the ratio of the extended to the compact R band fluxes and the ratio of the cold plus very cold component to the warm emission component. The conclusion was that the warm emission component is related with the central regions of the galaxies while the cold and the very cold emission had to originate in the disk of these galaxies.

b) Furthermore, a correlation has been found between the flux produced by the warm component and the flux in the high ionization coronal lines fluxes like $[\text{OIV}]\lambda 25.9$ and $[\text{NeV}]\lambda 14.3\mu\text{m}$ (Prieto, Pérez García & Rodríguez Espinosa 2000), indicating that the warm component must be heated by the nucleus of these galaxies.

c) In another recent paper, Pérez García et al. (2000) have shown that based on 90 μm ISO maps of four nearby Seyferts, the 90 μm emission is physically extended up to radii similar or larger than those seen in optical images of these same galaxies. Furthermore, the extension of this 90 μm emission has been characterized and its extension, scale length and surface brightness profiles are typical of normal galaxy disks.

Based on the above, a scenario arises in which the warm component is associated with dust heated by

radiation coming from the nuclear or circumnuclear regions of these galaxies, while the cold and very cold dust must be heated by process occurring in the galaxy disk. Danese et al. (1992) also conclude that the mid IR emission (10-25 μm) is dominated by the nucleus or the circumnuclear region. Further support to this scenario comes from the following:

- Warm dust. Its characteristic peak temperature is in the range 120-170 K, a range of temperatures warmer than is normal of dust in typical starforming regions. The nuclear origin of the radiation responsible for the heating of the warm dust was already indicated by Rudy (1984) who found a correlation between the [OIII] λ 5007 emission line flux and the 10 μm emission for a sample of quasars, Seyfert galaxies and radiogalaxies. This author suggested that the dust responsible for the 10 μm emission is mixed with the ionized gas of the Narrow Line Region (NLR) that produces the [OIII] λ 5007 emission line. More recently, Giuricin, Mardiossian and Mezzetti (1995) support the idea of the nuclear heating of this warm dust, based on 10 μm small aperture observations of a sample of 100 galaxies. They found that the 10 μm emission correlates very well with the 25 μm IRAS emission, while the correlation is poor with the 60 μm emission. From a different perspective Heckmann et al. (1997) have found in the Seyfert 2 galaxy Mrk 477 a strong starburst with very warm dust in an scale of a few hundred parsecs, that confirms the idea that the warm dust can also be heated by nuclear and circumnuclear starformation regions.
- Cold dust. Peak temperatures for this component range between 40 and 70 K, a range of temperatures that is typical of dust in regions of starformation. Note that cold dust is present in mostly all classes of galaxies, including normal and starburst galaxies (Knapp et al. 1996; Chini, Kruger & Kreysa 1992; Klaas et al 1997; Walterbos & Schwering 1987). In all these galaxy types, the heating of the dust is produced by OB stars in star formation regions in the galaxy disks. The higher temperatures corresponding to higher recent starformation rates (Young et al. 1989)
- Very cold dust. Peak temperatures for this component range from around 15 to 25 K, temperatures that are normal of dust heated by the general interstellar radiation field. This very cold dust is typically composed of big grains in thermal equilibrium with the interstellar radiation field and has been observed in normal spiral galaxies (see, e.g., Walterbos & Greenewalt 1996; Walterbos & Schwering 1987; Cox, Kruger & Metzger 1986). For example, Cox, Kruger & Metzger (1986) predict that the dust of the Galaxy is at a temperature of around 15-20 K, and Walterbos & Schwering show that in the disk of M31 there is very cold dust at 21 K.

4.1. NGC 1068

NGC 1068 has been observed at a wider spectral range than the rest of the sample, 11 filters between 4 and 200 μm have been employed. NGC 1068 is indeed one of the best studied Seyfert 2 galaxies in all spectral ranges. Morphologically it is classified as SAb, and was the first galaxy in which broad emission lines in polarized light were found (Miller & Antonucci 1983; Antonucci and Miller 1985). In the IR range, Tresh-Frenberg et al. (1987) have found that the emission between 5 and 20 μm presents an elongated structure in the nucleus, that they explain as thermal emission by dust heated by both the active nucleus and an active starforming region near ($1''$ - $2''$) the nucleus. The comparison between 10 μm images and HST images (Cameron et al. 1993) indicates a correlation between the hot dust emission and the Narrow Line Region. These authors developed a model that replaces the molecular torus by giant molecular clouds of gas and dust that attenuate the broad lines. Braatz et al. (1993) found a correlation between a 12.4 μm image and both optical continuum and [OIII] images; they also observed that the IR emission is aligned perpendicular to the torus plane and inferred that the extended IR emission is thermal radiation by dust in molecular clouds heated by collimated nuclear emission, without ruling out a possible contribution by dust in the molecular torus. Telesco & Harper (1980) have studied the far IR emission of NGC 1068 with KAO (Kuiper Airborn Observatory) observations between 30 and 300 μm and have found two thermal components with temperatures of ~ 36 K and ~ 115 K.

We have applied the inversion method explained before in the same spectral range that we have used for the rest of the objects in the sample, i.e., between 12 and 200 μm . Figure 3 shows the results obtained, i.e., two thermal components, a cold one with peak temperature of $T \sim 36$ K and a warm one with $T \sim 115$ K in the peak. It remains however to extend the fit to the shorter wavelength data which we have for NGC 1068 alone. When we apply the inversion method to the full range observed (4-200 μm) the SED of NGC 1068 appears now as the sum of three thermal components (see Figure 3). Two of them can be identified with the two thermal components previously found before without considering the 4-12 μm range. The peak temperatures of the three components are now 29, 110 and 278 K. The differences between the flux contained in each of the two components common to both inversions is less than 7%.

EDITOR: PLACE FIGURE 3 HERE.

The three components found in NGC 1068 are explained as in the rest of the objects of the CfA sample. The cold component is produced by dust in the host galaxy, the warm component corresponds to dust

heated by the active nucleus and/or circumnuclear starforming regions. The dust at higher temperature is also heated by the active nucleus, and should either be located in the inner part of the torus or be heated by active starforming regions placed in a radius <100 pc from the active nucleus (González Delgado et al. 1998). The flux enclosed under the component with $T \sim 278$ K is $F = 9.17 \cdot 10^{-9}$ erg cm $^{-2}$ s $^{-1}$, and the corresponding luminosity $L = 2.40 \cdot 10^{45}$ erg s $^{-1}$, while the total IR luminosity of NGC 1068 is $8.60 \cdot 10^{45}$ erg s $^{-1}$. Hence this component represents 28% of the total IR luminosity, which agrees with the fraction of the total UV emission that is produced by circumnuclear starforming regions in a sample of Seyfert 2 galaxies (González Delgado et al. 1998).

5. Energy balance: The cold emission component

One possible test that can confirm the suggestion made before on the relation between the cold emission component and the presence of starforming regions in the galaxy discs consists of testing the ratio of H α emission to far IR output. For instance in NGC 3079, the observed H α luminosity is $7.93 \cdot 10^{40}$ erg sec $^{-1}$ (Armus, Heckman & Miley 1990), a figure that includes both the nuclear and extended H α luminosity. Moreover, with a ratio of extended to nuclear H α emission of 0.77 (Armus, Heckman & Miley 1990), the extended H α emission amounts to $3.49 \cdot 10^{40}$ erg sec $^{-1}$, which shows the importance of the H α flux produced in star forming regions outside the central region in this object. If we take as an average extinction the value measured by Hawarden et al. (1995) $A_V=7.5$ mag, the extinction at H_α is $A_{H_\alpha}=6.1$ mag, and the extinction corrected extended H α luminosity is $0.93 \cdot 10^{43}$ erg sec $^{-1}$. This is to be compared with the IR output due to dust in starforming regions that competes with the gas for high energy photons from massive stars. In NGC 3079 this is what we have called the cold emission (Pérez García, Rodríguez Espinosa & Santolaya Rey 1998), which amounts to $3.52 \cdot 10^{44}$ erg sec $^{-1}$, or a ratio of H α to cold FIR emission of 0.03. This value is in agreement with the expected value in regions where massive stars are forming (Devereux & Young 1990). Hence for NGC 3079 there is good agreement between the H α output from disk HII regions and the cold IR emission, which confirms the results in Pérez García et al. (1998) and in this work indicating that the cold component emission in Seyfert galaxies originates in starforming regions within their disk.

In the case of NGC 4051 we consider the ratio between H α and far IR luminosity in two limiting cases. First, we consider the total integrated H α luminosity, $4.34 \cdot 10^{41}$ erg sec $^{-1}$ (Romanishin 1990), which after correction for extinction ($A_V=0.24$, Ho et al. 1997) becomes $5.22 \cdot 10^{41}$ erg sec $^{-1}$. Hence, the ratio of total

H α to cold far IR emission ($0.25 \cdot 10^{44}$ erg sec $^{-1}$) is 0.02. This is an upper limit as the total H α emission includes the nuclear emission which to a certain extent can be due to non-thermal processes associated with the AGN. On the other hand, if we consider the H α emission coming exclusively from the star-forming regions in the disk of NGC 4051, which according to González Delgado et al. (1997) is 26% of the total emission we get a ratio of extended H α to cold far IR emission of 0.006. This is a lower limit as some of the H α flux that we have assumed nuclear is very likely due to extended circumnuclear emission that will also contribute to the cold far IR emission. The actual value for the ratio of extended H α flux to cold far IR emission ranges therefore between 0.006 and 0.02, a value that is well within the range given by Devereux & Young (1990) as typical of normal HII regions in the disk of spiral galaxies.

In the case of NGC 5033 the integrated H α flux is $3.98 \cdot 10^{41}$ erg sec $^{-1}$ (Kennicutt 1983), which after correcting for extinction ($A_V = 1.48$, Ho et al. 1997) becomes $1.20 \cdot 10^{42}$ erg sec $^{-1}$. The H α emission to cold far IR emission ratio is 0.02, which is again to be taken as an upper limit given that the total H α flux includes the nuclear emission which we can not separate because we do not have the necessary data, However this upper limit is similar to that obtained for NGC 4051.

As for the rest of the sample a similar exercise with H α fluxes obtained from the literature produce similar results. In very few instances have we been able to separate the extended from the nuclear H α emission. For these cases the ratio of extended H α emission to cold far IR emission ranges between $1 \cdot 10^{-5}$ for NGC 5929 and 0.02 for Mrk 270. In most cases this separation between extended and nuclear emission has not been possible and hence ratios between the total H α emission and the cold far IR output have been obtained. These range between $1.5 \cdot 10^{-4}$ (Mrk 766) and $2 \cdot 10^{-3}$ (NGC 3516). In all cases it can be seen that the ratios are within those expected if massive stars are responsible for the ionizing photons as well as for the heating of the dust. We therefore conclude that the cold emission component that appeared naturally from the inversion process is related to radiation from dust in starforming regions in the galaxy discs.

6. Seyfert type differences

The current understanding of Seyfert galaxies assumes that the differences between the two Seyfert types are due to geometric factors in the nuclear region. If this is so we should look for differences in the warm emission component between the Seyfert types. Let us therefore turn our attention to the warm dust component that we have suggested it is directly related to the nuclear and circumnuclear dust emission. If

there is a molecular torus obscuring the nuclear region and this is sufficiently thick (as the models predict, see e.g. Pier & Krolik 1992; Granato & Danese 1994) we shall observe differences in the warm component emission produced by each of the two Seyfert types.

In order to compare the parameters obtained from the inversion of the SEDs for the different Seyfert types, we establish two different groups of objects within the CfA sample: Seyfert 1s, including galaxies classified as Seyfert 1.5, and Seyfert 2s, including Seyfert 1.8 and 1.9. Therefore, the sample gets divided into 22 Seyfert 1 and 24 Seyfert 2. If we drop those objects not observed or those whose data do not allow obtaining a well defined warm component, the sample with adequate data for this analysis consists of 18 Seyfert 1 galaxies and 22 Seyfert 2 galaxies.

If the dust responsible for the warm emission component is located within the molecular torus that hides both the active nucleus and the broad line region, we expect to find differences between some of the parameters that define the warm component of the Seyfert 1 and 2 objects. If however the dust is located outside the molecular torus, then the geometry does not play anymore a key role and we should not see differences between the two types of Seyfert galaxies.

6.1. Temperature differences

Regarding the temperature distribution, it should be realized that in both Seyfert classes we are sampling dust emission produced under similar physical conditions, probed with the same wavelength range, and heated in either case by the active nucleus or by circumnuclear starforming regions. Therefore as temperature is an intensive quantity as opposed to extensive, we expect not to see any difference between the average temperature of the warm component in the two Seyfert types.

Figure 4 shows the distribution of warm component temperature for the two groups of Seyfert galaxies. It is seen that the median temperature of the Seyfert 1s is slightly higher than the median of the Seyfert 2s though the differences are small, IZw1 excepted. As we pointed out before, IZw1 is a special object, its warm temperature being way far out of every other object in the sample. We have therefore dropped IZw1 from the statistics. To understand the significance of the differences between the two distributions, we have applied a Kolmogorov-Smirnov (KS) test. The characteristics of the distributions are:

$$\begin{aligned}\langle T \rangle_1 &= 148 \quad \sigma = 12. \\ \langle T \rangle_2 &= 144 \quad \sigma = 14.\end{aligned}$$

The result of this KS test is that there is a 78% probability that the two distributions are the same and so the differences between them are not significant and both groups (Seyfert 1 and Seyfert 2) enjoy, as expected, the same temperature distribution.

6.2. Fluxes and luminosities

Recent studies of the mid IR emission from Seyfert galaxies claim that Seyfert 2 galaxies are weaker than Seyfert 1s (Heckman 1995; Maiolino et al. 1995; Giuricin, Mardirossian & Mezzeti 1995; Mulchaey et al. 1994). This result is interpreted within the framework of the unified models as an anisotropy, resulting from the presence of a molecular torus with a given optical thickness in the IR. To test this claim we have compared the fluxes and luminosities of the warm component of the Seyfert SEDs to see if we find significant differences between Seyfert 1 and Seyfert 2s.

The median values for the warm luminosities are:

$$\begin{aligned}\langle \log L_{warm} \rangle_1 &= 44.7 \quad \sigma = 0.3 \\ \langle \log L_{warm} \rangle_2 &= 44.9 \quad \sigma = 0.8\end{aligned}$$

Statistically, the KS test shows that there is a probability 33% that both distributions are the same. Hence there are no significant differences between the Seyfert 1 and 2's regarding the warm emission.

Turning now to the total far IR luminosities, i.e., the sum of the three emission components, the distributions are:

$$\begin{aligned}\langle \log L_{IR} \rangle_1 &= 45.1 \quad \sigma = 0.8 \\ \langle \log L_{IR} \rangle_2 &= 44.9 \quad \sigma = 0.7\end{aligned}$$

In this case the distributions are the same with a significance level of 99% therefore it can not be concluded that the Seyfert 1s are brighter than the Seyfert 2s in the mid and far IR.

We now turn to search whether there are differences between Seyfert 1 and Seyfert 2s in the ratio of warm component to total luminosity. First, we refer to the ratios between the warm and total fluxes. The mean and standard deviations of these distributions are:

$$\begin{aligned}\langle F_{warm}/F_{IR} \rangle_1 &= 0.42 \quad \sigma = 0.17 \\ \langle F_{warm}/F_{IR} \rangle_2 &= 0.28 \quad \sigma = 0.15\end{aligned}$$

Figure 4 shows the flux ratio distributions. A KS test indicates that the distributions are different at the 99% level of significance. This result suggests that the Seyfert 1s emit fractionally more than the Seyfert 2s in the mid IR (warm component). This is consistent, for example, with the models of circumnuclear tori of Pier & Krolik (1992;1993) and of Granato & Danese (1994), that predict anisotropy by absorption of nuclear emission in the mid IR. However this result should be taken with care, as it could indicate either that the nuclear emission is larger in the Seyfert 1s relative to their total FIR flux or that the contribution of the host galaxy is stronger in the Seyfert 2s. To discriminate between these two possible explanations we must normalize the infrared fluxes with an isotropic property of the galaxies in the sample, i.e., with fluxes emitted at long enough wavelengths that they are not suspect of suffering extinction and thus do not depend on the geometry of the sources. Other authors have used $[\text{OIII}]\lambda 5000 \text{ \AA}$ fluxes, hard X-ray fluxes or radio fluxes (see, for example, Mulchaey et al. 1994). However, the $[\text{OIII}]\lambda 5000 \text{ \AA}$ fluxes can be affected by absorption due to dust in the NLR. We prefer to use 20 cm radio emission fluxes to normalize the IR flux, since the radio emission is not affected by selective extinction. We have used integrated radio data from Edelson (1987). These data consists of VLA observations at 1.46 GHz (20 cm) with a bandwidth of 45 MHz. The FWHM beamwidth used is 1.5 arcmin, directly comparable with our ISO data.

The distributions of the radio normalized warm IR fluxes show the following characteristics:

$$\begin{aligned} \langle \log(F_{warm}/F_{20cm}) \rangle_1 &= 6.5 \quad \sigma = 0.3 \\ \langle \log(F_{warm}/F_{20cm}) \rangle_2 &= 6.1 \quad \sigma = 0.3 \end{aligned}$$

KS tests indicate that both distributions are different at a significance level of 99.9%. Therefore, the warm flux is indeed higher in Seyfert 1s than it is in Seyfert 2s, and it can be concluded that the warm emission from Seyfert 2s is affected by dust extinction to a larger extent than in the Seyfert 1 galaxies.

This result suggests that at shorter wavelengths (mid IR) the emission is still anisotropic, in agreement with the molecular torus models of Pier & Krolik (1992;1993) and Granato & Danese (1994). These and others authors have proposed different models for the absorbing material. Pier & Krolik (1992;1993), Granato & Danese (1994) and Efstathiou & Rowan-Robinson (1994) have modeled the absorbing structures as axially symmetric tori. The models proposed by Granato & Danese (1994) result in thin and extended tori with optical depths ranging from $\tau \approx 10$ to 300 in the UV band and maximum radii ranging from tens to hundreds of parsecs. On the contrary, the models proposed by Pier & Krolik (1993) show thin

and compact accretion disks with very large optical depths with values of $\tau \lesssim 1000$ in the UV band, and compact radii with dimension of a few pc. If we consider the Seyfert 1 as canonical unobscured objects, and ascribe the differences found between the two Seyfert types to absorption by the obscuring torus we obtain a mid IR optical depth of $\tau_{IR} \approx 0.4$ or a $\tau_{UV} \approx 80$ (assuming $\tau_\lambda \propto 1/\lambda$) for the Seyfert 2 objects. This value is indeed very mild and within the range predicted for the thin and extended tori of Granato, Danese & Franceschini (1997).

The validity of ratioing with the 20 cm radio flux has been however questioned based on the idea that Seyfert 2 galaxies may have more star formation in their disks than Seyfert 1s (Maiolino et al. 1995). This would affect the radio emission, and hence the warm to radio flux ratio. It remains to test whether the Seyfert 2 galaxies are indeed stronger emitters of extended far IR radiation. We consider for this test the ratio of the cold far IR component to 20 cm radio flux. For the two groups the values are:

$$\begin{aligned} \langle \log(F_{cold}/F_{20cm}) \rangle_1 &= 6.7 \quad \sigma = 0.7 \\ \langle \log(F_{cold}/F_{20cm}) \rangle_2 &= 6.5 \quad \sigma = 0.5 \end{aligned}$$

These distributions are similar (60% probability) according to the KS test. Therefore, Seyfert 2s are not stronger emitters in extended IR radiation than Seyfert 1s, and there are no reasons to suspect that they should be stronger radio emitters based solely on the amount of star formation occurring in Seyfert 2s. It is also worth pointing out that the differences found between the type 1 and 2 Seyferts are restricted to the warm emission, while there are not differences regarding the cold and very cold emission, i.e., the emission from their respective galaxy disks.

7. Summary

We have presented far IR photometry with ISO of the CfA Seyfert sample. The data have allowed a detailed study of the far IR SED of these sources using a Bayesian inversion method. It has been shown that the mid and far IR emission of Seyfert galaxies can be explained by the emission of three thermal components, a warm component, associated with dust heated by the nucleus and circumnuclear starformation regions; a cold dust component heated by star forming region in the galaxy disk, and very cold dust component heated by the general interstellar radiation field. The mid to far IR output from Seyfert galaxies does not have a simple origin but different ingredients play an important role in it.

The comparison of cold far IR fluxes with $H\alpha$ data confirms that the cold emission component that appeared naturally from the inversion process is related to radiation from dust in starforming regions in the galaxy discs.

We find that the mid IR emission (warm component) is larger in Seyfert 1 than in 2s, suggesting the presence of obscuring material in Seyfert 2s. The median value obtained for the optical depth is in the range predicted by the thin and extended tori models.

REFERENCES

- Antonucci, R.J.J., Miller, J.S., 1985, *ApJ*, 297, 621
- Armus, L., Heckman, T.M., Miley, G.K., 1990, *ApJ*, 364, 471
- Bonatto, C.J., Pastoriza, M.G., 1997, *ApJ*, 486, 132
- Boroson, T.A., Meyers, K.A., 1992, *ApJS*, 80, 109
- Braatz, J.A., Wilson, A.S., Gezari, E.Y., Varosi, J., Beichman, C.A., 1993, *ApJ*, 409, L5
- Bregman, J.N., 1990, *A&A Rev*, 2, 125
- Cameron, M., Storey, J.W.V., Rotaciuc, V., Genzel, R., Verstraete, L., Drapatz, S., Siebenmorgen, R., Lee, T.J., 1993, *ApJ*, 419, 136
- Chini, R., Kruger, E., Kreysa, E., 1992, *A&A*, 315, 75
- Cox, R., Kruger, E., Mezger, P.G., 1986, *A&A*, 155, 380
- Danese, L., Zitelli, V., Granato, G.L., Wade, R., De Zotti, G., Mandolesi, N., 1992, *ApJ*, 399, 38
- Devereux, N.A., Young, J.S., 1990, *ApJ*, 350, L25
- Edelson, R.A., 1987, *ApJ*, 313, 651
- Edelson, R.A., Malkan, M.A., Rieke, G.H., 1987, *ApJ*, 321, 233
- Efstathiou, A., Rowan-Robinson, M., 1994, *MNRAS*, 212, 218
- Giuricin, G., Mardirossian, F., Mezzetti, M., 1995, *ApJ*, 446, 550
- González Delgado, R.M., Pérez, E., Tadhunter, C., Vilchez, J.M., Rodríguez Espinosa, J.M., 1997, *ApJS*, 108, 155
- González Delgado, R.M., Heckman, T., Leitherer, C., Meurer, G., Krolik, L., Wilson, A., Kinney, A., Koratkar, A., 1998, *ApJ*, 505, 174
- Goodrich, R.W., 1989, *ApJ*, 342, 234

- Granato, G.L., Danese, L., 1994, MNRAS, 268, 233
- Granato, G.L., Danese, L., Franceschini, A., 1997, ApJ, 487, 147
- Halpern, J.P., Moran, E.C., 1998, ApJ, 494, 194
- Hawarden, T.G., Israel, F.P., Geballe, T.R., Wade, R., 1995, MNRAS, 276, 119
- Heckman, T.M., 1995, ApJ, 446, 101
- Heckman, T.M., González-Delgado, R.M., Leitherer, C., Meurer, G.R., Krolik, J., Wilson, A.S., Koratkar, A., Kinney, A., 1997, ApJ, 482, 114
- Huchra, J., Burg, R., 1992, ApJ, 393, 90
- Kennicutt, R.C. Jr., 1983, ApJ, 272, 54
- Kessler, M. F., Steinz, J.A., Anderegg, M.E., Clavel, J., Drechsel, G., Estaria, P., Faelker, J., Riedinger, J.R., Robson, A., Taylor, B.G., Ximenez de Ferran, S., 1996, A&A, 315, L27
- Klaas, U., Haas, M., Heinrichsenm, J., Schulz, B., 1997, A&A, 325, L21
- Knapp, G.R., Rupen, M.P., Fich, M., Harper, D.A., Wynn-Williams, C.G., 1996, A&A, 315, L75
- Lawrence, A., Elvis, M., Wilkes, B.J., McHardy, I., Brandt, N., 1997, MNRAS, 285, 879
- Lemke, D., et al. 1996, A&A, 315, L64
- Lonsdale, C.J., Helou, G., Good, J.C., Rice, W., 1984, “Cataloged galaxies and quasars observed in the IRAS survey”
- Maiolino, R., Krabbe, A., Thatte, N., Genzel, R., 1998, ApJ, 493, 650
- Maiolino, R., Ruiz, M., Rieke, G.H., Keller, L.D., 1995, ApJ, 446, 101
- Miller, J.S., Antonucci, R.J.J., 1983, ApJ, 271, 7
- Mulchaey, J.S., Koratkar, A., Ward, M.J., Wilson, A.S., Whittle, M., Antonucci, R.J.J., Kinney, A.L., Hurt, T., 1994, ApJ, 436, 658
- Neugebauer, G., 1978, PhyS, 17, 149

- Osterbrock, D.E., Pogge, R.W., 1985, ApJ, 297, 166
- Prieto, M.A., Pérez García, A.M., Rodríguez Espinosa, J.M., 1999 (in preparation)
- Pérez García, A.M., Rodríguez Espinosa, J.M., Fuensalida, J.J., 1998, ApJ (submitted)
- Pérez García, A.M., Rodríguez Espinosa, J.M., Santolaya Rey A.E., 1998, ApJ, 500, 685
- Pier, E.A., Krolik, J.H., 1993, ApJ, 418, 673
- Pier, E.A., Krolik, J.H., 1992, ApJ, 401, 99
- Rieke, G.H., 1978, ApJ, 226, 550
- Rieke, G.H., Low, F.J., 1972, ApJ, 176, L95
- Rigopoulou, D., Papadakis, I., Lawrence, A., Ward, M., 1997, A&A, 327, 493
- Rodríguez Espinosa, J.M., Pérez García, A.M., Lemke, D., Meisenheimer, K., 1996, A&A, 315, L129
- Rodríguez Espinosa, J.M., Pérez García, A.M., 1997, ApJ, 487, L33
- Rodríguez Espinosa, J.M., Rudy, R.J., Jones, B., 1987, ApJ, 312, 555
- Romanishin, W., 1990, AJ, 100, 373
- Rudy, R.J., 1984, ApJ, 284, 33
- Salas, L., 1992, ApJ, 385, 288
- Siebenmorgen, R., Moorwood, A., Friedling, W., Kaeufl, H.U., 1997, A&A, 325, 450
- Simpson, C., Wilson, A.S., Bower, G., Heckman, T.M., Krolik, J.H., Miley, G.K., 1997, ApJ, 474, 121
- Smith, M.A., Lada, C.J., Thronson, H.A., Glaccum, W., Harper, D.W., Loewenstein, R.F., Smith, J., 1983, ApJ, 274, 571
- Spinoglio, I., Malkan, M.A., Rush, B., Carrasco, L., Recillas-Cruz, E., 1995, ApJ, 453, 616
- Stein, W.A., 1975, PASP, 87, 5

Telesco, C.M., 1990, in “Infrared Astronomy”, Mampaso, A. Prieto, M., Sánchez, F., Eds., Cambridge University Press, p173

Telesco, C.M., 1988, ARA&A, 26, 343

Telesco, C.M., Harper, D.A., 1980, ApJ, 235, 392

Tresh-Frenberg, R., Fazio, G.G., Gezari, D.Y., Lamb, G.M., Shu, P.K., Hoffmann, W.F., McReight, C.R., 1987, ApJ, 312, 542

Walterbos, R.A.M., Greenwalt, B., 1996, ApJ, 460, 696

Walterbos, R.A.M., Schwering, P.B.W., 1987, A&A, 180, 27

Wilson, A.S., Braatz, J.A., Heckman, T.M., Krolik, J.H., Miley, G.K., 1993, ApJ, 419, L61

Young, J.S., Xie, S., Kenney, J.D.P., Rice, W.L., 1989, ApJS, 70, 699

Fig. 1.— Spectral Energy Distributions of the CfA Seyfert sample. Fluxes are in Janskys

Fig. 2.— Mid and far IR SEDs of the CfA Seyfert sample. For each object, the upper panel shows the ISO (triangles) and IRAS (filled squares) data and the best fit to the SED obtained with the Planckian inverse transform. The different thermal components contributing to the fit are printed in dashed lines. The bottom panel shows the temperature spectrum responsible for these components

Fig. 3.— Mid and far IR Spectral Energy Distribution of NGC 1068. As in Figure 2, ISO data are triangles and IRAS data are filled squares. Top: The two thermal components obtained with the inversion method are plotted with dashed lines. In this case, we have not considered the two first shortwavelength data points in order that the spectral range are equal to the rest of CfA sample. Bottom: Result after applying the inversion method to all the complete data set.

Fig. 4.— Top: Distribution of temperatures of the warm components for the objects of the CfA sample. Note that the value of IZw1 is clearly higher than the rest of the temperatures. Bottom: Distribution of the ratio between the warm and the total fluxes of the CfA sample

Table 1. ISO fluxes (in Janskys) for the CfA Seyfert sample

Object	16 μ m	25 μ m	60 μ m	90 μ m	120 μ m	135 μ m	180 μ m	200 μ m
Mkr 334	0.39	0.83	6.44	7.93	2.41	1.66	0.38	0.35
Mkr 335	0.24	0.36	0.71	0.43	(²)	(²)	(²)	(²)
0048+29 ¹								
IZw 1	0.64	1.08	3.42	2.43	1.30	0.79	0.45	(²)
Mkr 993	0.13	0.09	0.34	0.77	0.47	0.17	0.43	0.39
Mkr 573	0.55	0.81	3.60	1.79	(²)	(²)	(²)	(²)
0152+06	0.25	0.24	1.19	1.79	4.21	4.19	1.57	1.33
Mkr 590	0.46	0.26	3.06	2.59	(³)	(³)	(³)	(³)
NGC 1144	0.46	0.75	8.21	14.70	22.04	22.39	14.22	12.04
Mkr 1243	0.21	(²)	0.25	0.28	0.94	1.150	1.01	0.62
NGC 3079	2.07	2.99	55.25	55.95	162.23	165.96	109.89	95.12
NGC 3227	1.22	2.07	13.57	12.35	30.45	34.38	25.87	23.43
NGC 3362	0.21	0.35	2.13	3.10	3.27	3.79	2.83	3.24
1058+45	0.13	0.28	0.81	1.81	2.25	2.61	1.74	1.38
NGC 3516	0.77	0.92	3.11	2.43	1.50	1.11	0.52	0.38
Mkr 744	0.19	0.39	1.20	1.53	5.93	6.23	4.31	3.97
NGC 3982	0.43	0.83	8.19	11.55	19.07	20.26	17.70	14.45
NGC 4051	1.44	2.17	7.65	11.85	47.31	54.22	38.11	36.90
NGC 4151	4.12	5.18	6.28	6.94	7.90	8.52	5.73	4.69
NGC 4235	0.17	0.28	0.65	0.66	0.19	0.74	0.57	0.30
Mkr 766	0.73	1.35	6.05	5.13	3.74	3.47	2.72	2.10
Mkr 205	0.19	0.27	0.69	1.25	2.24	3.00	2.64	3.20
NGC 4388	1.55	3.40	11.63	16.44	24.28	28.20	19.07	16.78
Mkr 231	3.96	6.90	76.27	61.45	37.72	26.67	15.97	13.34
NGC 5033	1.34	1.78	18.77	32.96	93.13	104.08	75.87	66.93
Mrk 789 ¹								
1335+39	0.13	0.24	1.80	2.39	2.39	2.95	1.78	1.64
NGC 5252	0.10	0.14	1.85	1.21	0.97	1.50	0.70	0.53

Table 1—Continued

Object	16 μ m	25 μ m	60 μ m	90 μ m	120 μ m	135 μ m	180 μ m	200 μ m
Mkr 266	0.33	1.07	9.72	11.11	11.60	9.41	6.98	5.11
Mkr 270	0.06	0.13	0.21	0.09	0.64	0.57	0.43	0.62
NGC 5273	0.09	0.18	1.24	1.95	1.18	1.19	0.96	0.63
Mkr 461	(²)	0.20	0.15	0.32	0.25	0.30	0.21	0.30
Mkr 279	0.29	0.50	1.58	2.20	2.54	2.62	1.46	1.59
IC 4397	0.16	0.22	2.43	3.69	4.17	4.36	2.82	1.65
NGC 5548	0.44	0.79	1.23	1.25	1.14	0.95	0.57	0.72
NGC 5674 ¹								
Mkr 817	0.49	1.11	4.71	3.80	1.49	1.37	0.62	0.69
Mkr 686 ¹								
Mkr 841	0.34	0.50	0.57	0.29	(²)	(²)	(²)	(²)
NGC 5929	0.55	1.50	13.11	16.01	19.50	17.32	10.33	7.39
NGC 5940 ¹								
1614+35	0.12	0.16	0.76	0.48	1.73	1.79	1.41	1.50
2237+07	0.25	0.35	0.50	0.54	0.70	0.71	0.51	0.22
NGC 7469	1.77	4.78	33.56	38.63	46.23	42.26	28.92	22.32
Mkr 530 ¹								
Mkr 533	0.86	1.75	4.58	6.32	7.63	7.61	6.63	3.75
NGC 7682	0.29	0.22	0.47	0.30	0.63	0.78	0.54	0.66

Note. — ¹ Not observed

² Not detected

³ Background not available

Table 2. Fluxes of NGC 1068. Fluxes are given in Janskys

$\lambda(\mu m)$	4.9	7.6	11.5	16	25	60	105	120	135	180	200
F (Jy)	6.9	16.7	44.0	46.9	92.6	212.4	331.2	360.6	288.3	155.2	120.8

Table 3. Central temperature of spectral components

Object	Type	Morph. type	T ₁ (K)	T ₂ (K)	T ₃ (K)
Mrk 334	2	Pec.		46	151
Mrk 335	1	S0/a	32	71	162
IZw1	1	S?	40	97	~300
Mrk 993	1.5	Sa	30	65	173
Mrk 573	2	SAB0	35	75	143
0152+06	2	SAb	22	43	153
Mrk 590 ²	1	SAA			
NGC 1068 ¹	2	SAb		36	115
NGC 1144	2	R	22	50	148
Mrk 1243	1	Sa	19	51	138
NGC 3079	L	SBC	22	42	152
NGC 3227	1.5	SABa	19	43	126
NGC 3362	2	SABc	20	42	113
1058+45	2	Sa	22	53	144
NGC 3516	1.5	SB0		42	148
Mrk 744	2	SABa	18	55	137
NGC 3982	2	SABb	20	42	124
NGC 4051	1	SABbc	20	49	148
NGC 4151	1	SABab	21	53	151
NGC 4235	1	SAA	16	38	145
Mrk 766	1.5	SBa	33	56	133
Mrk 205	1	SBab	16	28	156
NGC 4388	2	SAb	21	43	119
Mrk 231	1	SAC		39	150
NGC 5033	2	SAC	21	44	147
1335+39	2	S?	28	53	156
NGC 5252	2	S0	20	56	167
Mrk 266	2	Pec.	27	45	130

Table 3—Continued

Object	Type	Morph. type	T ₁ (K)	T ₂ (K)	T ₃ (K)
Mrk 270	2	S0	18	55	161
NGC 5273	1	SA0	31	63	151
Mrk 461	2	S	20	63	153
Mrk 279	1	S0	24	46	153
IC 4397	2	S?	26	46	158
NGC 5548	1	SA0	23	51	152
Mrk 817	1	S?		45	135
Mrk 841	1.5	E		71	162
NGC 5929	2	Sab	28	54	126
1614+35	1.5	S?	19	41	150
2237+07	2	SBa	22	58	151
NGC 7469	1	SABa	27	60	140
Mrk 533	2	SAbc	21	54	149
NGC 7682	2	SBab	16	45	136

Note. — ¹ Short wavelength data (5-11 μ m) not taken into account (See section 4.1)

Table 4. Fluxes for each component of the SEDs ($\text{erg cm}^{-2}\text{s}^{-1}$). F_1 corresponds to the **very cold** component, F_2 to the **cold** component and F_3 to the **warm component**. F_{total} is the total sum of the fluxes

Object	Type	F_1	F_2	F_3	F_{total}
Mrk 334	2		$2.964 \cdot 10^{-10}$	$9.618 \cdot 10^{-11}$	$3.655 \cdot 10^{-10}$
Mrk 335	1	$1.326 \cdot 10^{-11}$	$2.357 \cdot 10^{-11}$	$4.211 \cdot 10^{-11}$	$7.894 \cdot 10^{-11}$
IZw1	1	$1.135 \cdot 10^{-10}$	$9.073 \cdot 10^{-11}$	$>1.345 \cdot 10^{-10}$	$>3.453 \cdot 10^{-10}$
Mrk 993	1.5	$2.072 \cdot 10^{-11}$	$0.793 \cdot 10^{-11}$	$2.322 \cdot 10^{-11}$	$5.187 \cdot 10^{-11}$
Mrk 573	2	$9.210 \cdot 10^{-11}$	$2.596 \cdot 10^{-11}$	$1.120 \cdot 10^{-10}$	$2.300 \cdot 10^{-10}$
0152+06	2	$7.836 \cdot 10^{-11}$	$1.823 \cdot 10^{-11}$	$4.062 \cdot 10^{-11}$	$1.372 \cdot 10^{-10}$
Mrk 590 ²	1				
NGC 1068	2		$1.170 \cdot 10^{-8}$	$1.198 \cdot 10^{-8}$	
NGC 1144	2	$5.131 \cdot 10^{-10}$	$1.702 \cdot 10^{-10}$	$1.012 \cdot 10^{-10}$	$7.845 \cdot 10^{-10}$
Mrk 1243	1	$2.187 \cdot 10^{-11}$	$1.209 \cdot 10^{-11}$	$2.188 \cdot 10^{-11*}$	$5.584 \cdot 10^{-11}$
NGC 3079	L	$2.929 \cdot 10^{-9}$	$1.344 \cdot 10^{-9}$	$4.283 \cdot 10^{-10}$	$4.701 \cdot 10^{-9}$
NGC 3227	1.5	$5.505 \cdot 10^{-10}$	$3.850 \cdot 10^{-10}$	$2.805 \cdot 10^{-10}$	$1.216 \cdot 10^{-9}$
NGC 3362	2	$5.168 \cdot 10^{-11}$	$9.518 \cdot 10^{-11}$	$5.533 \cdot 10^{-11*}$	$2.022 \cdot 10^{-10}$
1058+45	2	$5.712 \cdot 10^{-11}$	$2.351 \cdot 10^{-11}$	$3.289 \cdot 10^{-11}$	$1.135 \cdot 10^{-10}$
NGC 3516	1.5		$1.201 \cdot 10^{-10}$	$1.593 \cdot 10^{-10}$	$2.794 \cdot 10^{-10}$
Mrk 744	2	$1.923 \cdot 10^{-10}$	$5.239 \cdot 10^{-11}$	$4.684 \cdot 10^{-11}$	$2.924 \cdot 10^{-10}$
NGC 3982	2	$3.597 \cdot 10^{-10}$	$2.951 \cdot 10^{-10}$	$1.121 \cdot 10^{-10}$	$7.669 \cdot 10^{-10}$
NGC 4051	1	$8.771 \cdot 10^{-10}$	$2.690 \cdot 10^{-10}$	$3.053 \cdot 10^{-10}$	$1.1.451 \cdot 10^{-9}$
NGC 4151	1	$1.519 \cdot 10^{-10}$	$2.961 \cdot 10^{-10}$	$8.346 \cdot 10^{-10}$	$1.282 \cdot 10^{-9}$
NGC 4235	1	$3.132 \cdot 10^{-12}$	$2.557 \cdot 10^{-11}$	$3.950 \cdot 10^{-11}$	$6.820 \cdot 10^{-11}$
Mrk 766	1.5	$1.537 \cdot 10^{-10}$	$1.187 \cdot 10^{-10}$	$1.741 \cdot 10^{-10}$	$4.465 \cdot 10^{-10}$
Mrk 205	1	$3.669 \cdot 10^{-11}$	$3.464 \cdot 10^{-11}$	$3.344 \cdot 10^{-11}$	$1.047 \cdot 10^{-10}$
NGC 4388	2	$4.980 \cdot 10^{-10}$	$4.286 \cdot 10^{-10}$	$4.540 \cdot 10^{-10}$	$1.380 \cdot 10^{-9}$
Mrk 231	1		$2.711 \cdot 10^{-9}$	$9.569 \cdot 10^{-10}$	$3.668 \cdot 10^{-9}$
NGC 5033	2	$1.822 \cdot 10^{-9}$	$4.121 \cdot 10^{-10}$	$2.586 \cdot 10^{-10}$	$2.502 \cdot 10^{-9}$
1335+39	2	$8.249 \cdot 10^{-11}$	$2.323 \cdot 10^{-11}$	$3.340 \cdot 10^{-11}$	$1.391 \cdot 10^{-10}$
NGC 5252	2	$2.250 \cdot 10^{-11}$	$2.232 \cdot 10^{-11}$	$2.812 \cdot 10^{-11}$	$7.294 \cdot 10^{-11}$
Mrk 266	2	$2.049 \cdot 10^{-10}$	$3.164 \cdot 10^{-10}$	$1.168 \cdot 10^{-10}$	$6.381 \cdot 10^{-10}$

Table 4—Continued

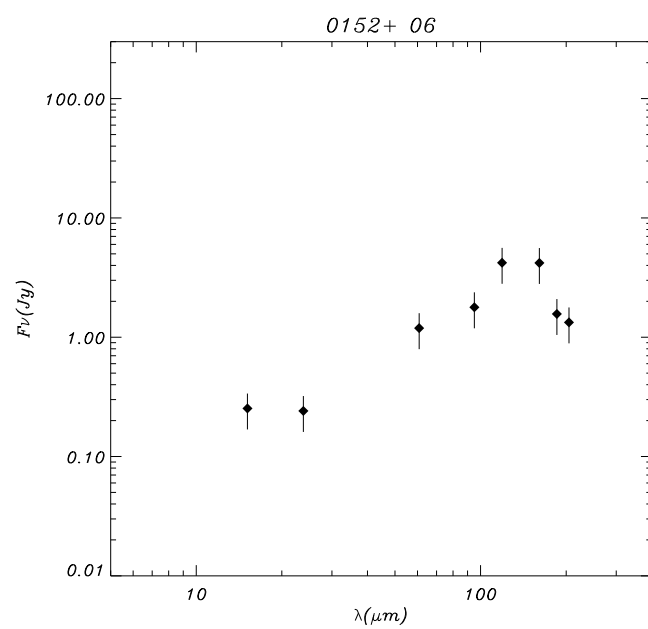
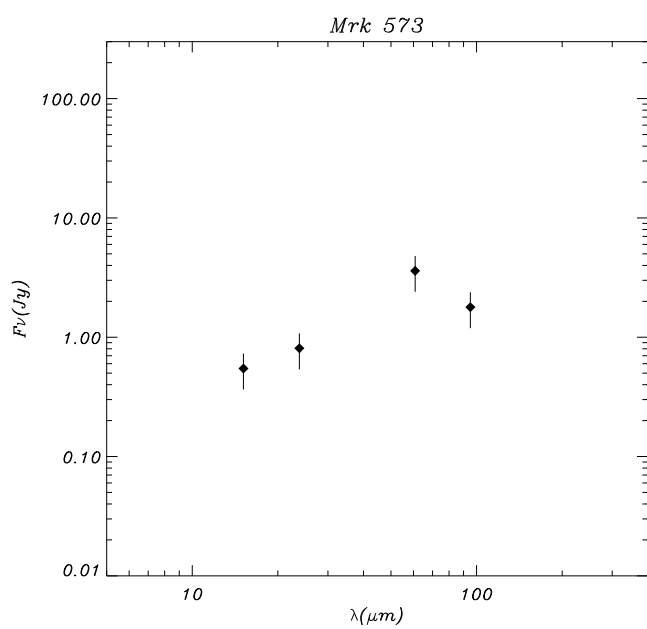
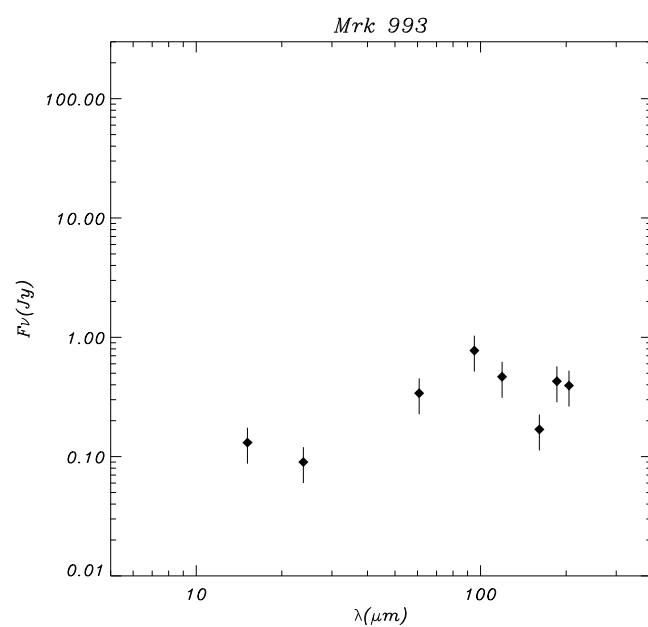
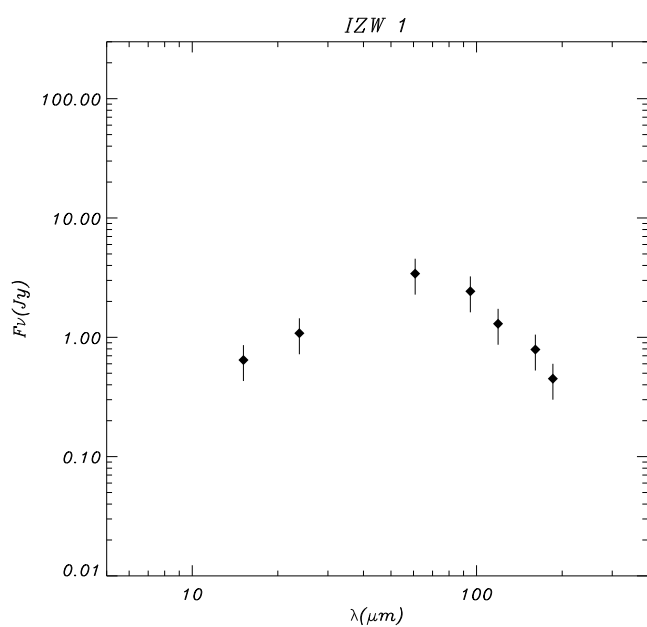
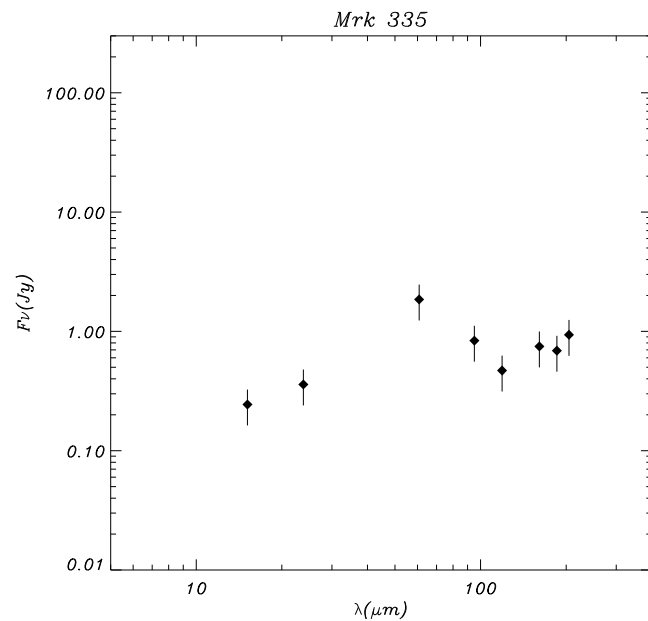
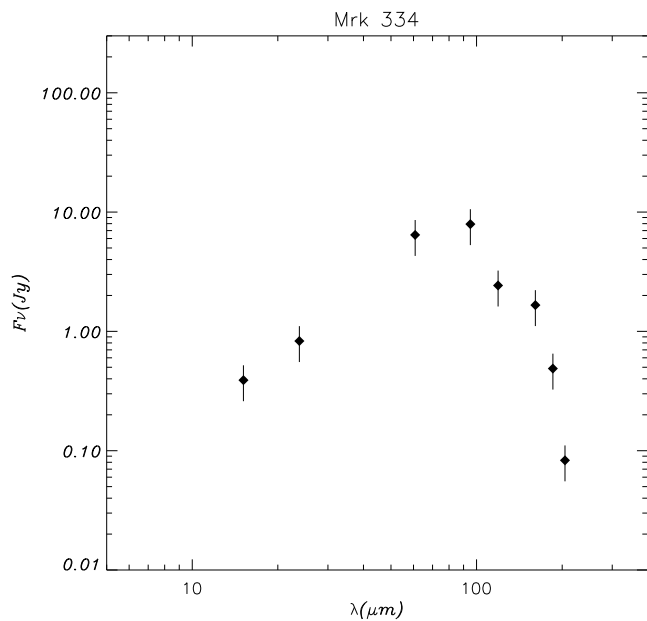
Object	Type	F_1	F_2	F_3	F_{total}
Mrk 270	2	$1.244 \cdot 10^{-11}$	$5.686 \cdot 10^{-12}$	$1.565 \cdot 10^{-11}$	$3.378 \cdot 10^{-11}$
NGC 5273	1	$5.174 \cdot 10^{-11}$	$3.219 \cdot 10^{-11}$	$1.576 \cdot 10^{-11}$	$9.969 \cdot 10^{-11}$
Mrk 461	2	$5.384 \cdot 10^{-12}$	$1.874 \cdot 10^{-11}$	$2.974 \cdot 10^{-11}$	$5.386 \cdot 10^{-11}$
Mrk 279	1	$7.046 \cdot 10^{-11}$	$3.165 \cdot 10^{-11}$	$6.831 \cdot 10^{-11}$	$1.704 \cdot 10^{-10}$
IC 4397	2	$1.194 \cdot 10^{-10}$	$3.566 \cdot 10^{-11}$	$3.635 \cdot 10^{-11}$	$1.913 \cdot 10^{-10}$
NGC 5548	1	$1.769 \cdot 10^{-11}$	$5.768 \cdot 10^{-11}$	$1.126 \cdot 10^{-10}$	$1.898 \cdot 10^{-10}$
Mrk 817	1		$1.680 \cdot 10^{-10}$	$1.357 \cdot 10^{-10}$	$3.037 \cdot 10^{-10}$
Mrk 841	1.5		$2.913 \cdot 10^{-11}$	$6,982 \cdot 10^{-11}$	$9.895 \cdot 10^{-11}$
NGC 5929	2	$5.487 \cdot 10^{-10}$	$2.282 \cdot 10^{-10}$	$1.654 \cdot 10^{-10}$	$9.423 \cdot 10^{-10}$
1614+35	1.5	$3.392 \cdot 10^{-11}$	$2.227 \cdot 10^{-11}$	$1.923 \cdot 10^{-11}$	$7.542 \cdot 10^{-11}$
2237+07	2	$1.297 \cdot 10^{-11}$	$3.840 \cdot 10^{-11}$	$5.347 \cdot 10^{-11}$	$1.048 \cdot 10^{-10}$
NGC 7469	1	$1.231 \cdot 10^{-9}$	$9.128 \cdot 10^{-10}$	$4.390 \cdot 10^{-10}$	$2.583 \cdot 10^{-9}$
Mrk 533	2	$1.532 \cdot 10^{-10}$	$2.594 \cdot 10^{-10}$	$2.217 \cdot 10^{-10}$	$6.643 \cdot 10^{-10}$
NGC 7682	2	$1.058 \cdot 10^{-11}$	$1.796 \cdot 10^{-11}$	$4.352 \cdot 10^{-11}$	$7.206 \cdot 10^{-11}$

Table 5. Luminosities for each component of the SEDs (10^{44}erg s^{-1}). L_1 corresponds to the **very cold** component, L_2 to the **cold** component and L_3 to the **warm component**. L_{IR} is the total luminosity

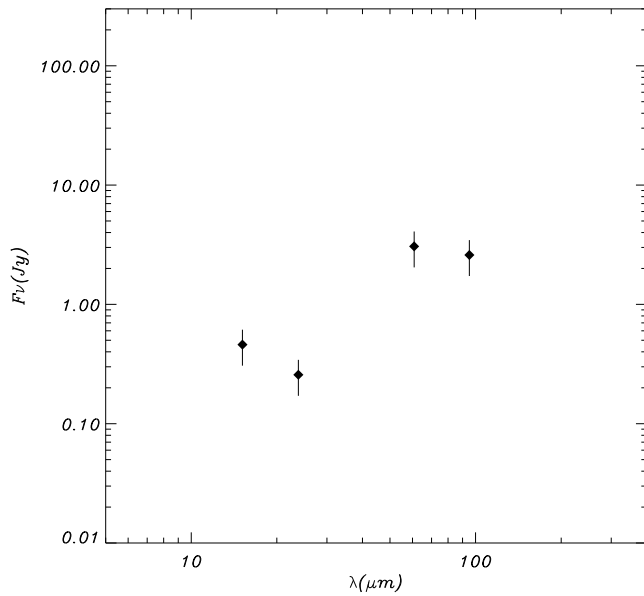
Object	Type	L_1	L_2	L_3	L_{IR}
Mrk 334	2		25.19	9.00	34.19
Mrk 335	1	1.72	3.06	5.47	10.25
IZw1	1	81.49	65.14	>96.57	>243.20
Mrk 993	1.5	0.94	0.36	1.06	3.76
Mrk 573	2	5.31	1.50	6.46	13.27
0152+06	2	4.57	1.06	2.37	8.10
Mrk 590 ²	1				
NGC 1068	2		30.06	31.93	61.99
NGC 1144	2	82.51	27.37	16.27	126.15
Mrk 1243	1	5.30	2.93	5.30	13.53
NGC 3079	L	7.68	3.52	1.12	12.32
NGC 3227	1.5	1.52	1.06	0.77	3.35
NGC 3362	2	5.15	9.48	5.51	20.14
1058+45	2	9.38	3.86	5.40	18.64
NGC 3516	1.5		1.67	2.21	3.88
Mrk 744	2	3.06	0.83	0.75	4.64
NGC 3982	2	0.62	0.51	0.19	1.32
NGC 4051	1	0.81	0.25	0.28	1.34
NGC 4151	1	0.26	0.51	1.44	2.21
NGC 4235	1	0.035	0.29	0.45	0.77
Mrk 766	1.5	4.84	3.74	5.49	14.07
Mrk 205	1	35.53	33.55	32.39	101.47
NGC 4388	2	6.12	5.26	5.58	16.96
Mrk 231	1		888.77	313.71	1202.48
NGC 5033	2	3.14	0.71	0.44	4.29
1335+39	2	6.43	18.12	26.05	50.60
NGC 5252	2	23.20	23.02	29.01	75.23
Mrk 266	2	30.02	46.37	17.11	93.50

Table 5—Continued

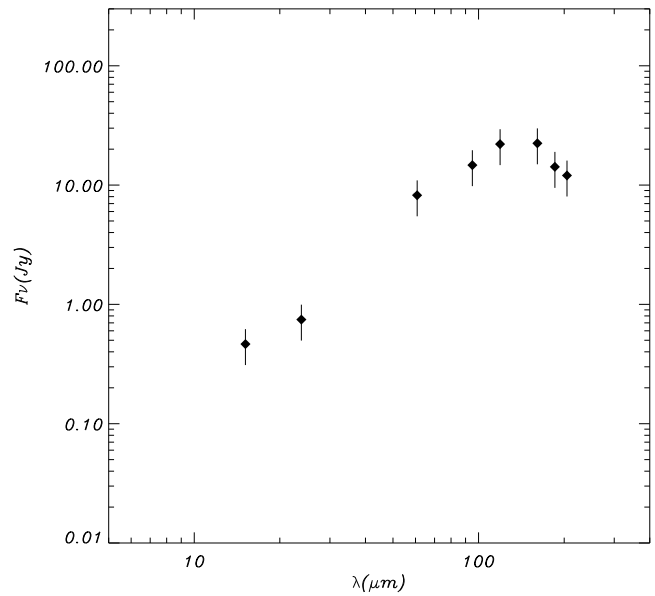
Object	Type	L ₁	L ₂	L ₃	L _{IR}
Mrk 270	2	0.19	0.09	0.24	0.52
NGC 5273	1	0.13	0.08	0.04	0.25
Mrk 461	2	0.27	0.92	1.47	2.66
Mrk 279	1	12.63	5.68	12.25	30.56
IC 4397	2	4.97	1.48	1.51	7.96
NGC 5548	1	0.94	3.06	5.98	9.98
Mrk 817	1		32.15	25.97	58.12
Mrk 841	1.5		7.51	18.00	25.51
NGC 5929	2	7.25	3.02	2.19	12.46
1614+35	1.5	5.15	3.38	2.92	11.45
2237+07	2	1.57	4.64	6.47	12.68
NGC 7469	1	60.72	45.02	21.65	127.39
Mrk 533	2	24.81	42.01	35.90	102.72
NGC 7682	2	0.59	1.00	2.42	4.01



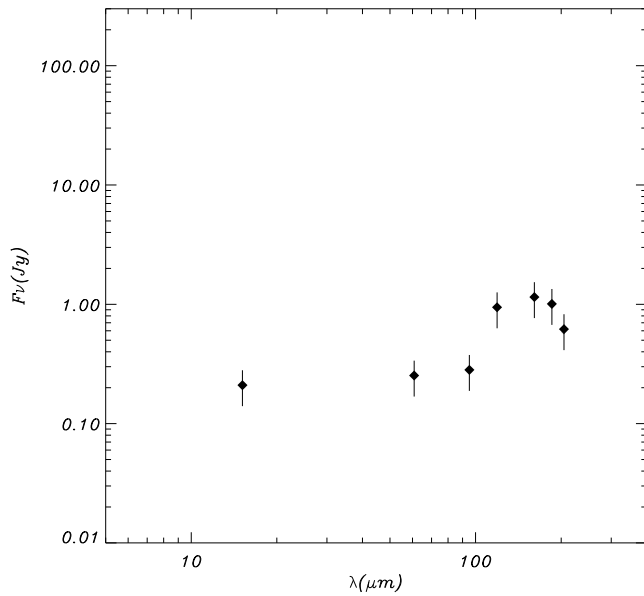
Mrk 590



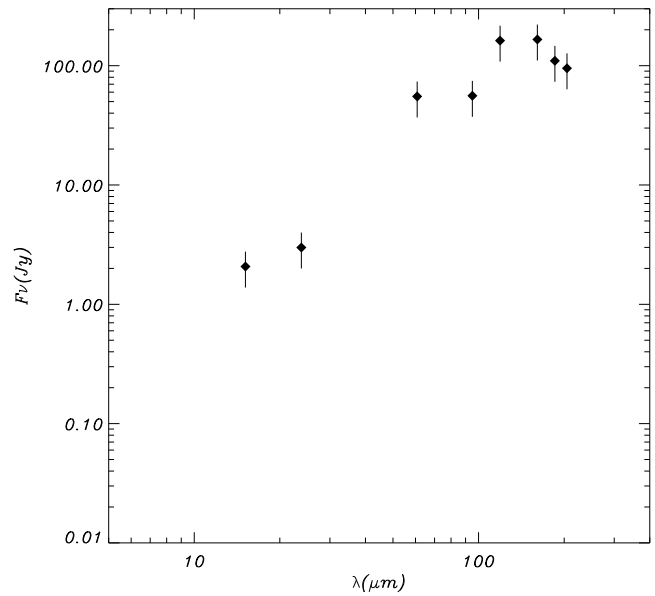
NGC 1144



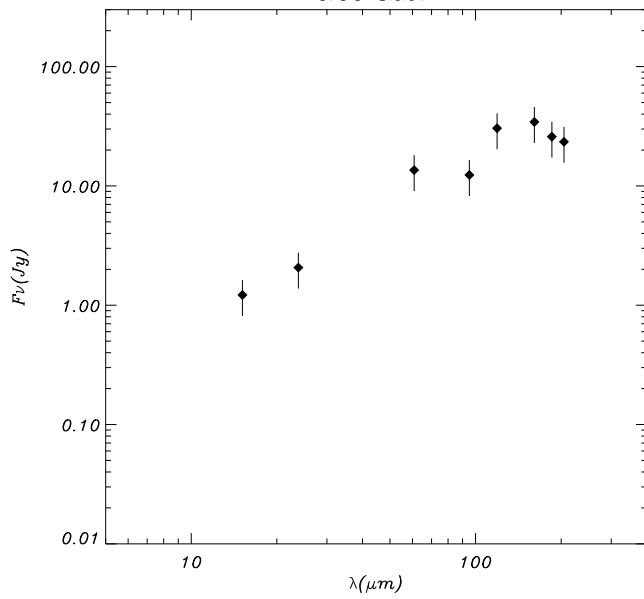
Mrk 1243



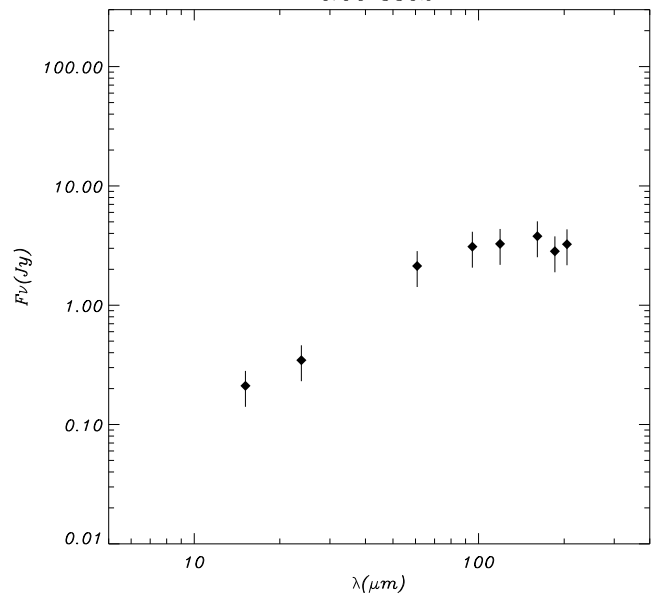
NGC 3079



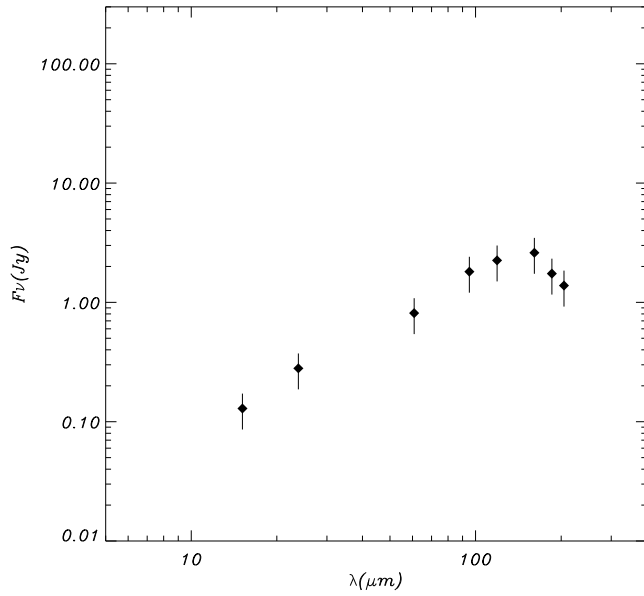
NGC 3227



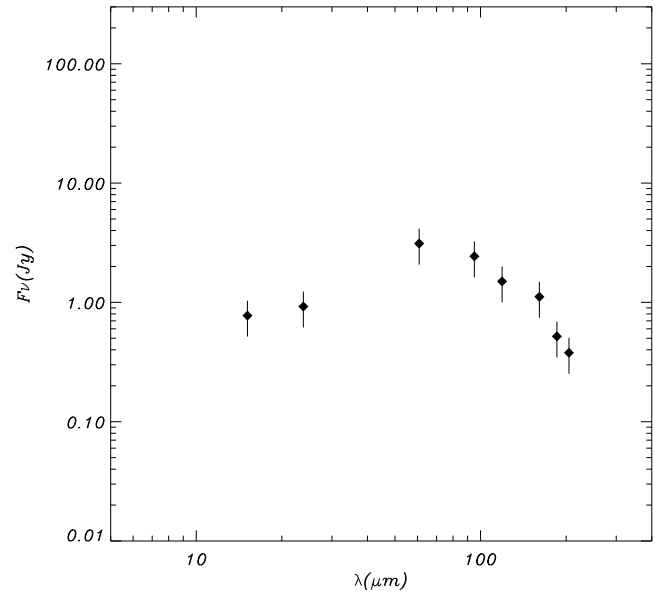
NGC 3362



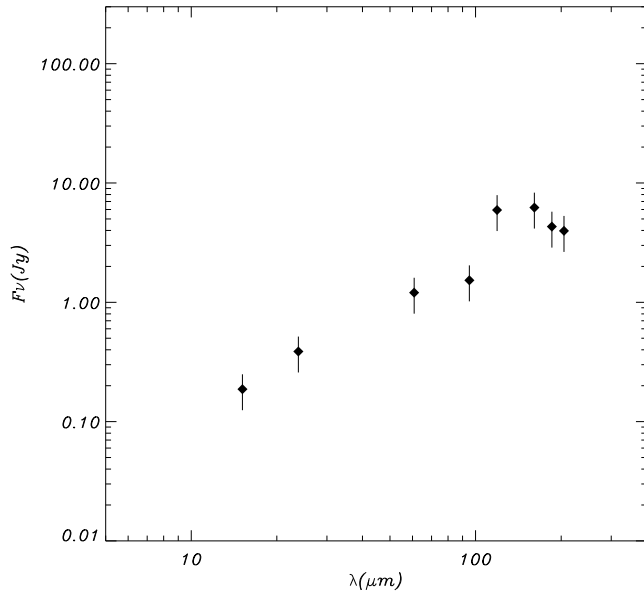
1058+ 45



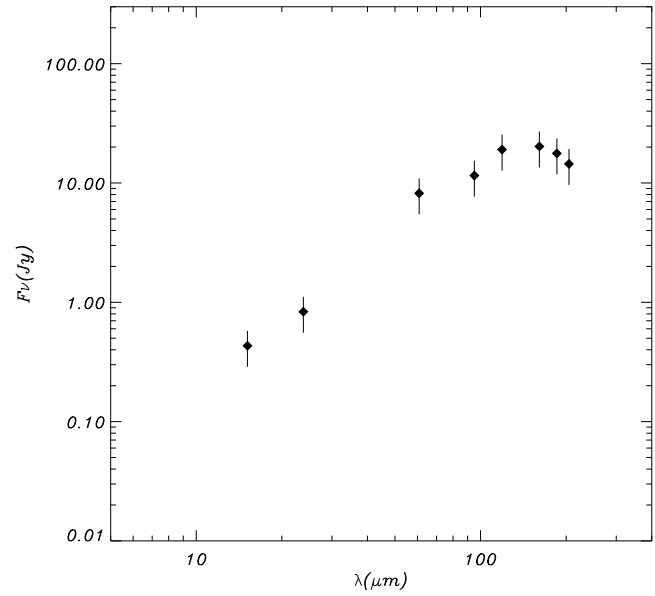
NGC 3516



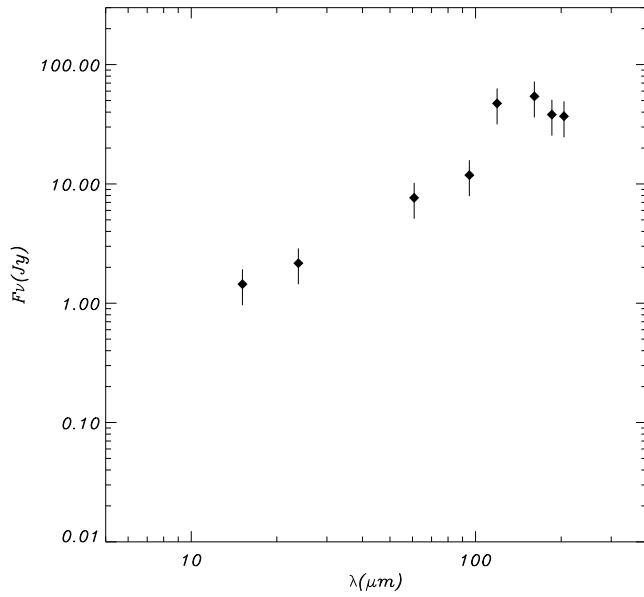
Mrk 744



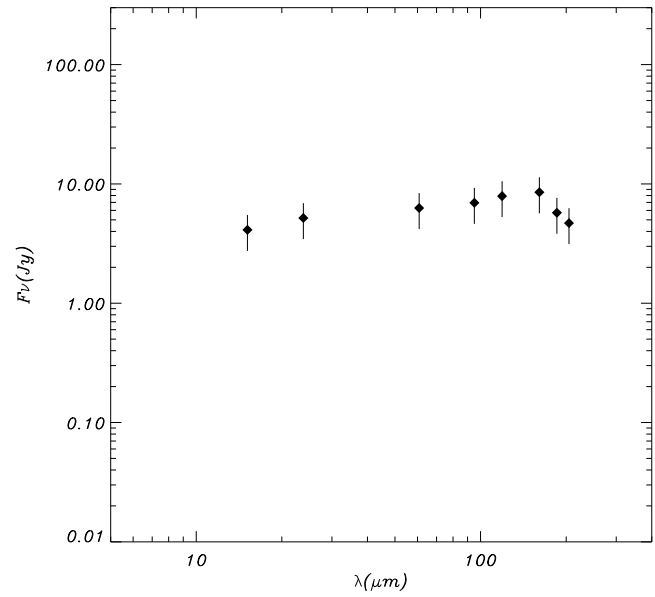
NGC 3982

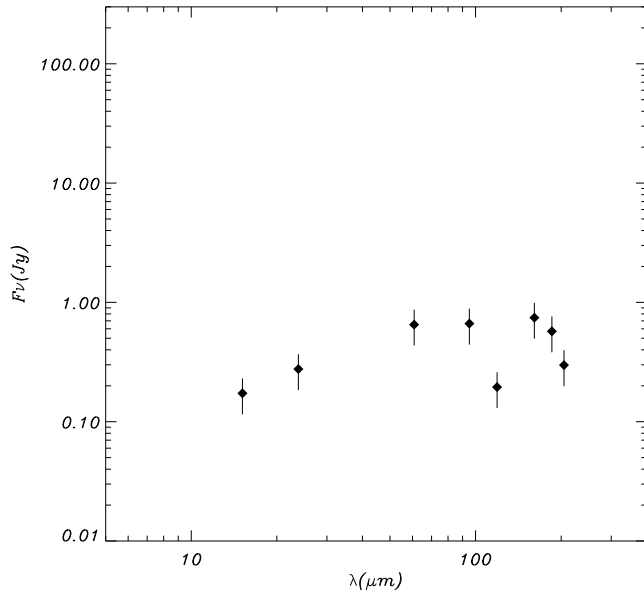
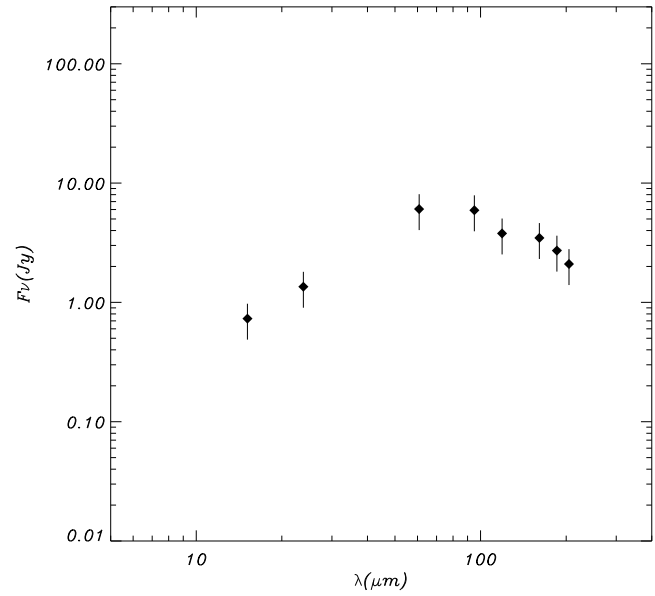
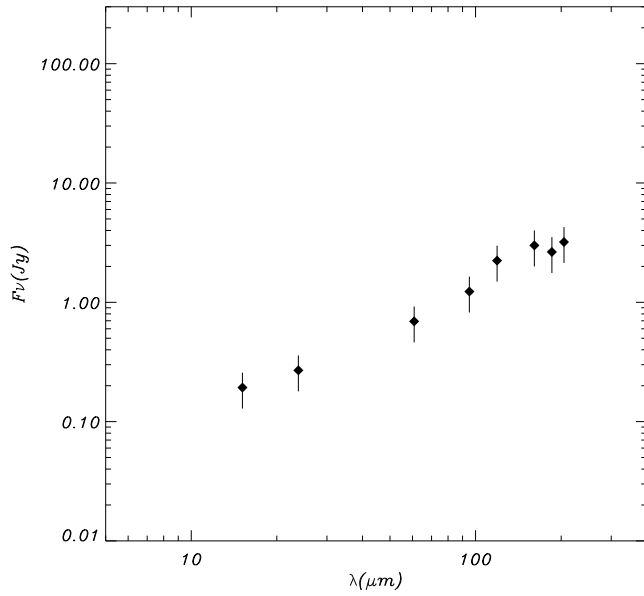
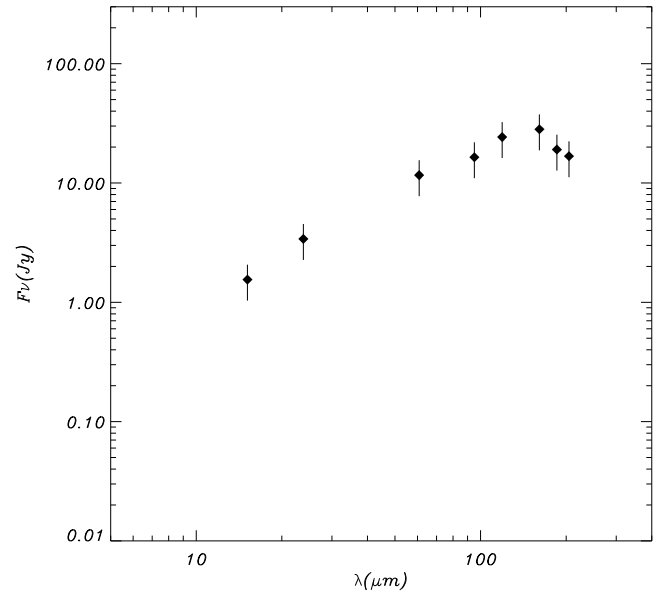
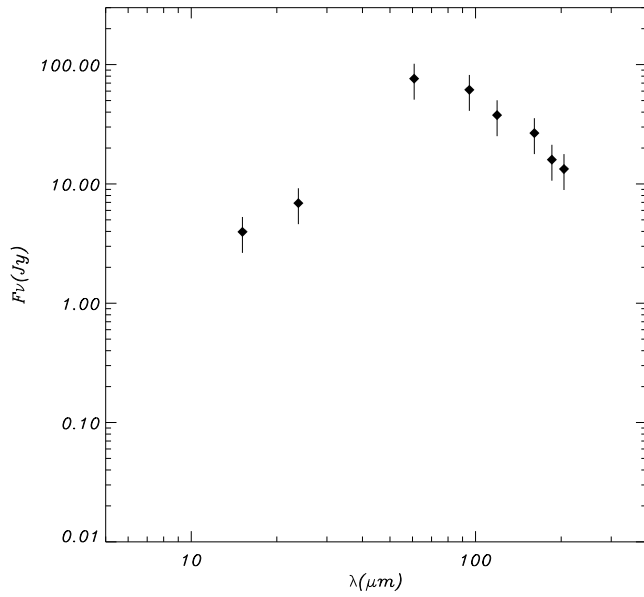
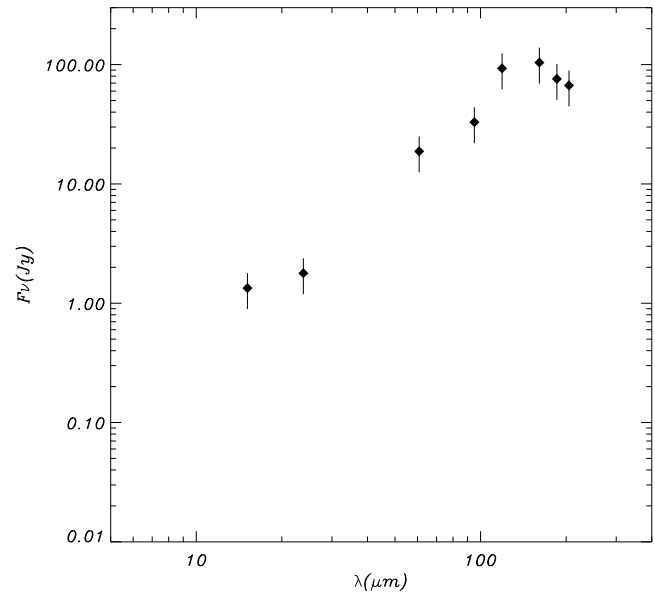


NGC 4051

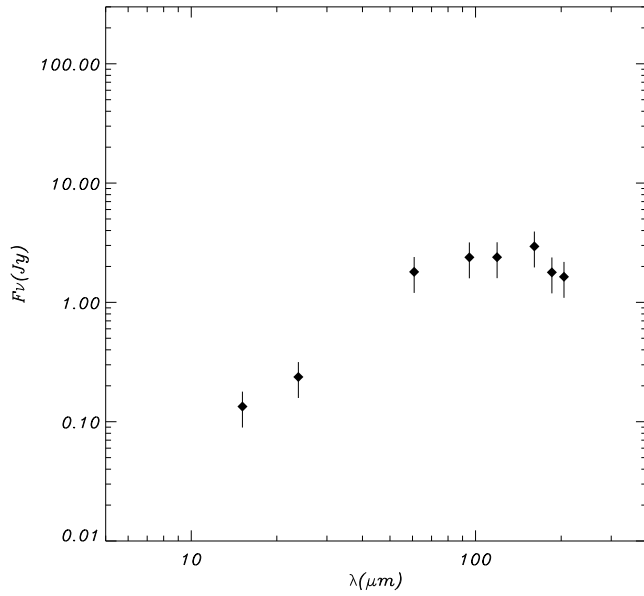


NGC 4151

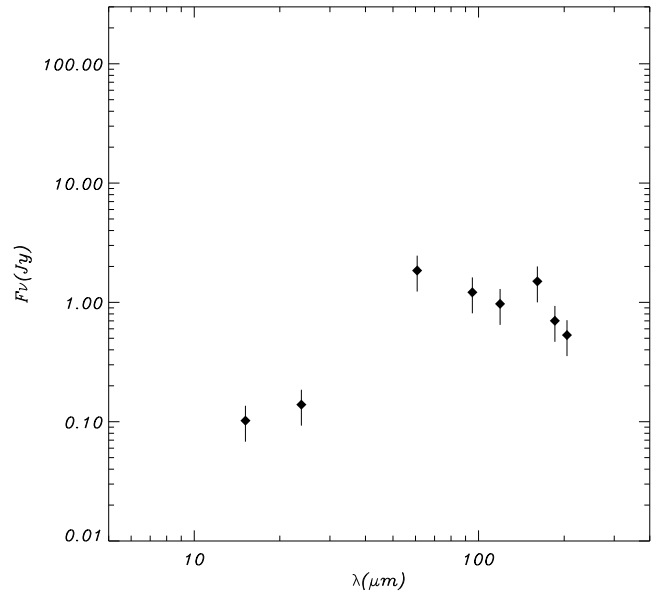


NGC 4235*Mrk 766**Mrk 205**NGC 4388**Mrk 231**NGC 5033*

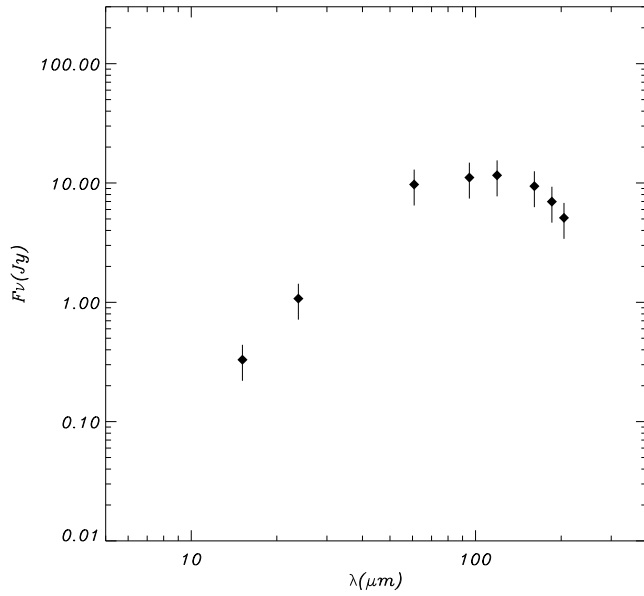
1335+ 39



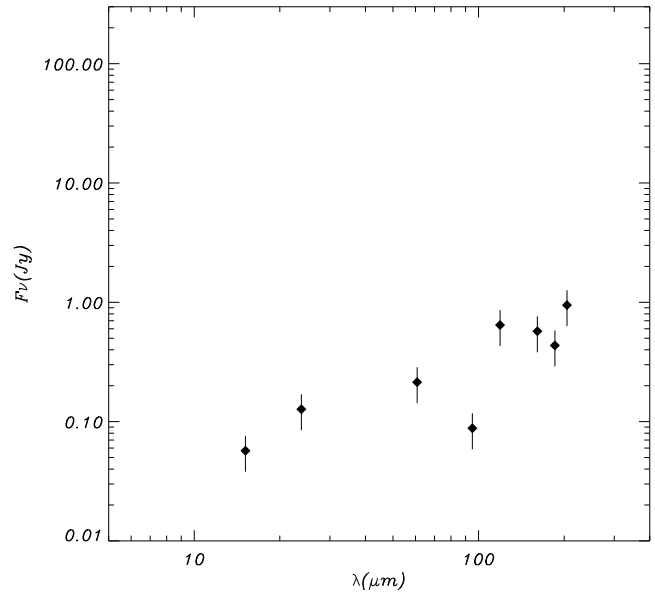
NGC 5252



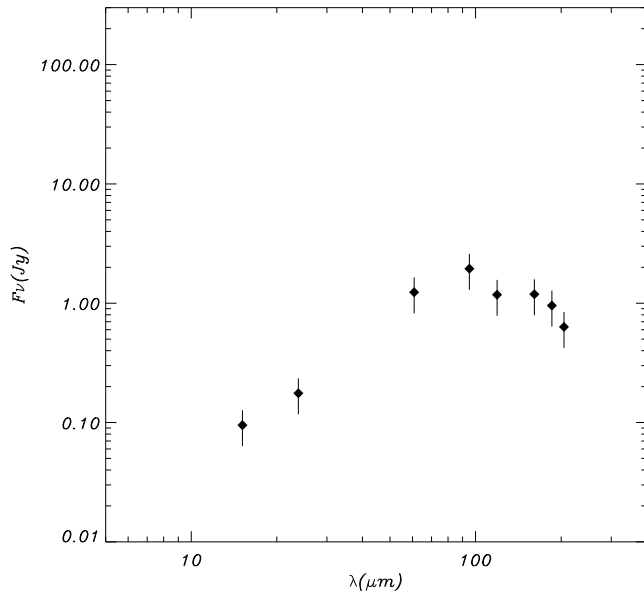
Mrk 266



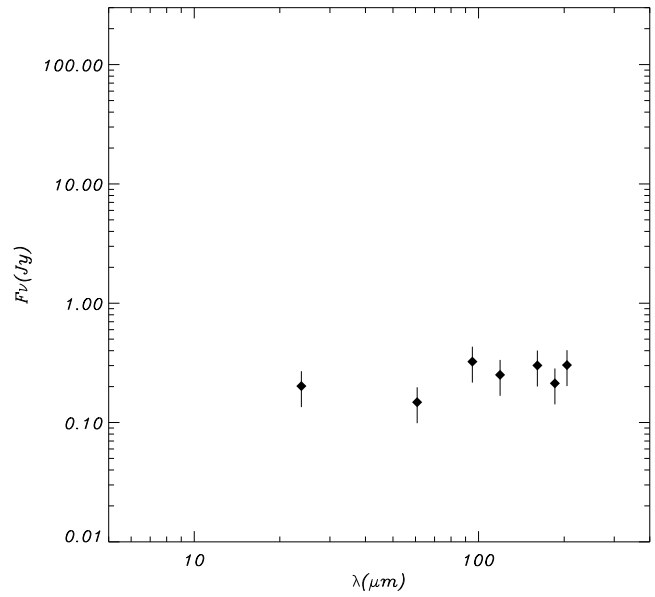
Mrk 270



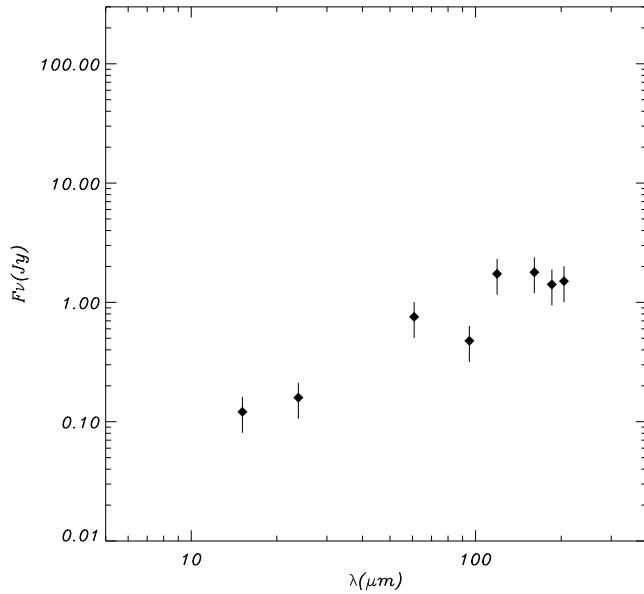
NGC 5273



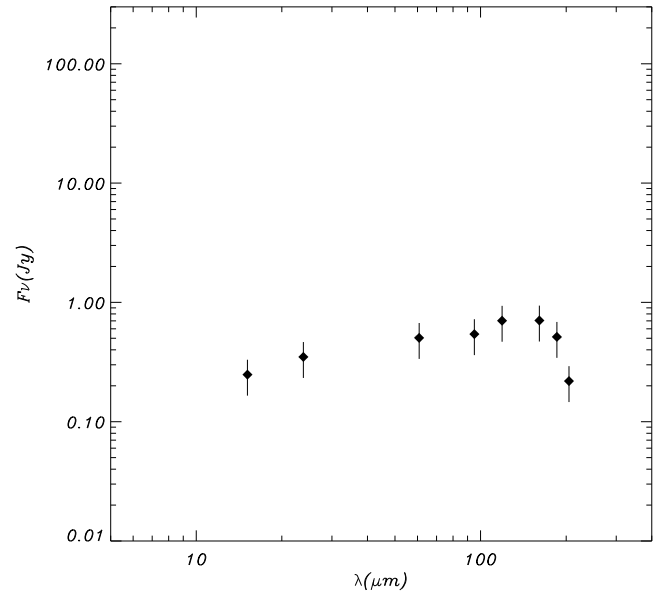
Mrk 461



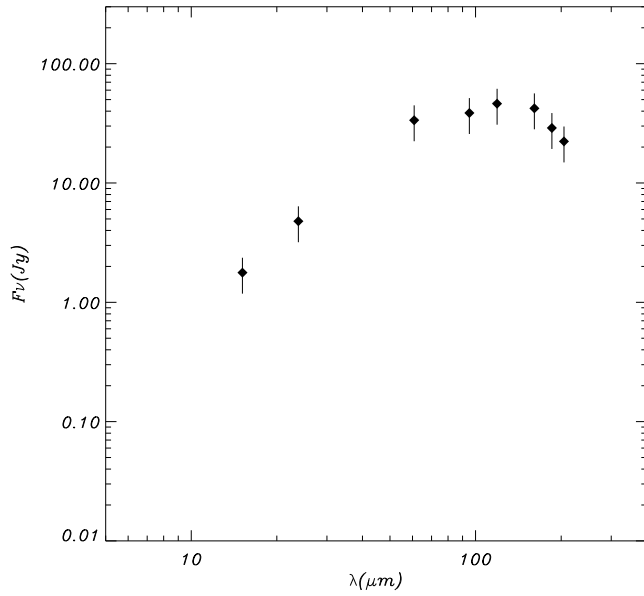
1614+ 35



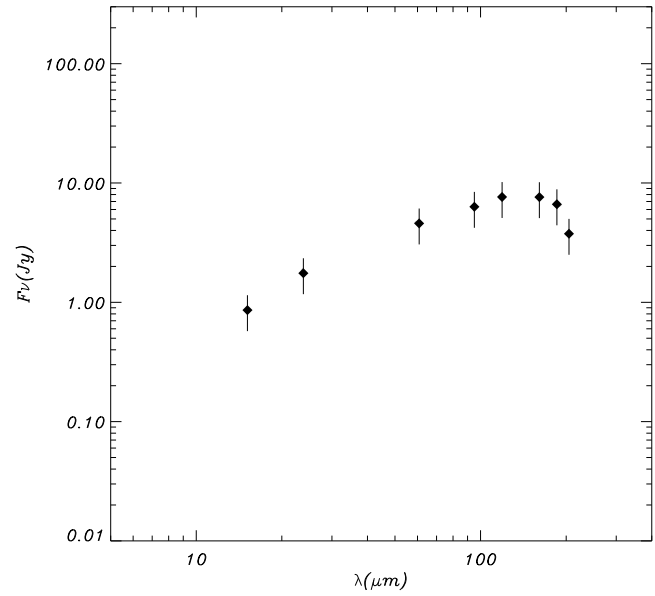
2237+ 07



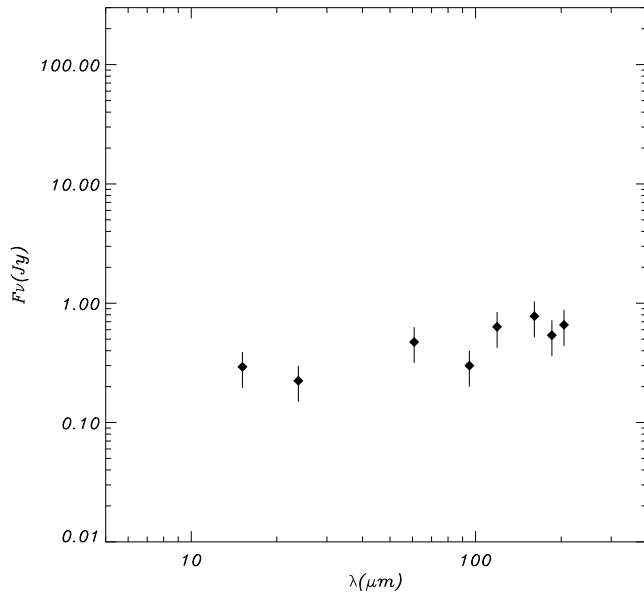
NGC 7469



Mrk 533



NGC 7682



NGC 1068

